ANL-09/13

Argonne NATIONAL LABORATORY

Study of Metallic Materials for Solid Oxide Fuel Cell Interconnect Applications

Nuclear Engineering Division

About Argonne National Laboratory

Argonne is a U.S. Department of Energy laboratory managed by UChicago Argonne, LLC under contract DE-AC02-06CH11357. The Laboratory's main facility is outside Chicago, at 9700 South Cass Avenue, Argonne, Illinois 60439. For information about Argonne and its pioneering science and technology programs, see www.anl.gov.

Availability of This Report

This report is available, at no cost, at http://www.osti.gov/bridge. It is also available on paper to the U.S. Department of Energy and its contractors, for a processing fee, from:

U.S. Department of Energy
Office of Scientific and Technical Information
P.O. Box 62
Oak Ridge, TN 37831-0062
phone (865) 576-8401
fax (865) 576-5728
reports@adonis.osti.gov

ANL-09/13

Study of Metallic Materials for Solid Oxide Fuel Cell Interconnect Applications

by
K. Natesan and Z. Zeng
Nuclear Engineering Division, Argonne National Laboratory

work supported at
Argonne National Laboratory by
The U.S. Department of Energy
Office of Industrial Technologies

March 2009

CONTENTS

FIGURES

TABLES

ABSTRACT

Metallic interconnect acts as a gas separator and a gas distributor and therefore, it needs to function adequately in two widely different environments. The interconnect material will be exposed to air on one side and natural gas or coal-derived synthesis gas on the other side. The viable material for the interconnect application must be resistant not only to oxidation but also carburization in hydrocarbon containing low-oxygen environments. In addition, the scales that develop on the exposed surfaces must possess adequate electrical conductivity for them to function as current leads over long service life of the fuel cell.

This report addresses five topics of interest for the development of metallic interconnects with adequate performance in fuel cells for long service life. The research conducted over the years and the conclusions reached were used to identify additional areas of research on materials for improved performance of components, especially metallic interconnects, in the complex fuel cell environments. This report details research conducted in the following areas: measurement of area specific electrical resistivity, corrosion performance in dual gas environments by experiments using alloy 446, long term corrosion performance of ferritic and austenitic alloys in hydrogen and methane-reformed synthesis fuel-gas environments, approaches to reduce the area resistance of metallic interconnect, and reduction of electrical resistivity of alumina scales on metallic interconnect. Based on the key requirements for metallic interconnects and the data developed on the corrosion behavior of candidate materials in meeting those requirements, several areas are recommended for further research to develop metallic interconnects with acceptable and reliable long-term performance in solid oxide fuel cells.

1. INTRODUCTION

Solid oxide fuel cells (SOFCs) are electrochemical reactors to convert chemical energy of the fuel to electrical energy. The key feature of SOFC is its high efficiency in energy conversion. Moreover, the effluent from SOFCs is much less polluting to the atmosphere than that of traditional energy generation methods. Therefore, the U.S. Department of Energy is funding the Solid State Energy Conversion Alliance (SECA) program to develop SOFCs for efficient conversion of fossil fuels with less pollution to the environment.[1-3]

At present, four different stack configurations have been proposed and fabricated for SOFCs: seal less tubular design, segment-cell-in-series design, monolithic design, and flat-plate design.[4] Among these designs, the flat-plate design offers high power density and simpler fabrication. In the flat-plate design of SOFC stack,[5] the individual cells are interconnected by an electrical conductor. Figure 1 shows a schematic of a flat-plate SOFC stack.

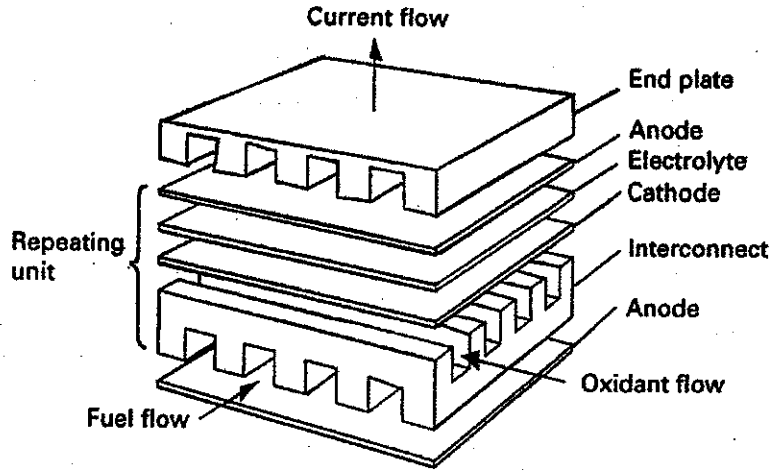

Figure 1. Schematic of the flat-plate design of a solid oxide fuel cell stack.[5]

1.1 Advantages of Metallic Interconnect

For high temperature SOFCs (with operating temperature ≈1000°C), ceramic materials such as, $La_{1-x}Ca_xCrO_3$ are considered for the fabrication of interconnects.[4] However, the ceramic interconnects are generally difficult to fabricate, less reliable, and subject to brittle fracture (especially under thermal cycling) which limit their application in SOFCs. Ceramic interconnects also exhibit poor thermal and electrical conductivity and are expensive since they incorporate rare-earth materials. Alternatively, research on metallic interconnect has been in progress since 1990.[6-8] The advantages of a metallic interconnect are reliability, lower cost, higher thermal and electrical conductivity, and ease of fabrication. However, traditional SOFCs operate at temperatures ≈1000°C which can render the metallic alloys to oxidize and lose their strength and mechanical integrity. In recent years, significant progress is being made to lower the operating temperature of the SOFCs to a range of 800-850°C by reducing the thickness of the electrolyte.[9,10] The lower operating temperature enables metallic materials as potential

candidates for interconnects and has attracted research in this area.[11-15] The objective of the research on metallic interconnects is to reduce the cost of fuel cell to the DOE target of $400 per kilowatt.[1-3]

1.2 Operating Environment of metallic Interconnect

Metallic interconnect acts as a gas separator and a gas distributor (see Fig. 1), therefore, it needs to function adequately in two widely different environments. The interconnect material will be exposed to air on one side and natural gas or coal-derived synthesis gas on the other side. On the air side, metallic interconnect needs protection from oxidation. On the other side with fuel gas, the interconnect needs to be protection from the carburizing gas. In the current fuel cell concepts, 550-850°C is proposed as the working temperature range for interconnect. In this temperature range, the alloy can not only carburize but also degrade by another catastrophic phenomenon known as "metal dusting."[15-19] Pits can initiate on alloy surface exposed to the environment and can grow with time leading to complete loss of metal. Figure 2 shows an example of metal dusting corrosion of a nickel-base Alloy 230.

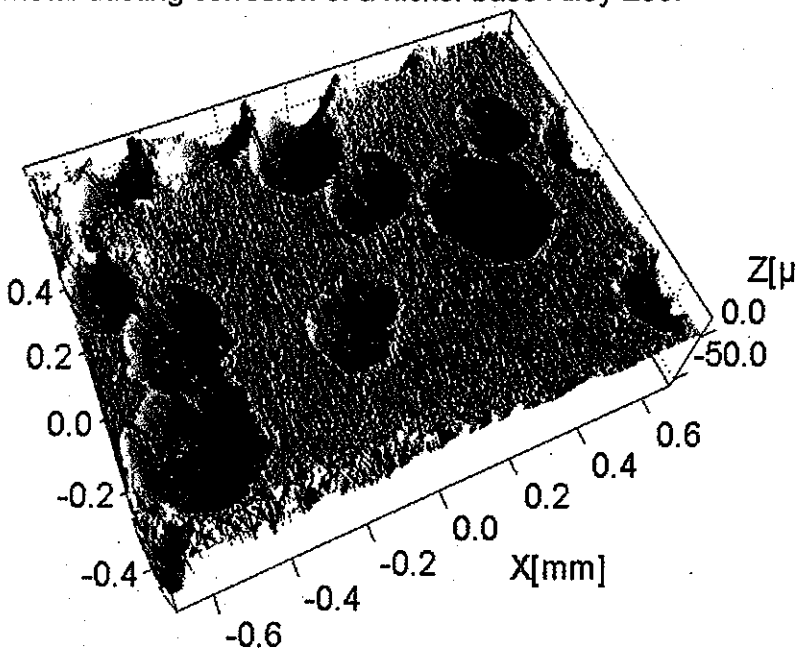

Figure 2. Corrosion pits on Alloy 230 after exposure in a carburizing gas at 600°C for 3,000 h.

Currently, natural gas (mainly methane) is oxidized in the fuel cell. The composition of the gas in the fuel side gradually changes from methane at the gas inlet to its oxidation products H_2+H_2O and CO+CO_2 at the outlet. If it is assumed that methane and its intermediate oxidation products are 90% oxidized in the fuel cell, the composition of the gas at the outlet will essentially be a mixture of CO and CO_2 (with a CO_2:CO ratio ≈9:1) and H_2 and H_2O (with a H_2O:H_2 ratio ≈15:1).[20] The steam content is low at inlet of fuel cell and will be high at the outlet of cell. Therefore, the atmosphere on the fuel side varies from carburizing at the inlet to slightly oxidizing at the outlet of fuel cell.

1.3 Requirements of Metallic Interconnect

i. The coefficient of thermal expansion (CTE) should be close to that of ceramic cell to minimize thermally induced stresses.

ii. The alloy should develop an adherent, continuous, slow-growing, protective surface oxide during exposure to air in the working temperature of 550-850°C, Corrosion by carbonaceous gas needs to be minimized.

iii. Acceptable electrical conductivity for the surface oxide scale.

iv. A negligible tendency for interfacial reactions with neighboring components.

v. The metal must be gas tight.

vi. The cost of the alloy must be sufficiently low to make the metallic interconnect and SOFC technology commercially feasible.

1.4 Technical Challenges Facing Metallic Interconnect

Metallic interconnect should be resistant to oxidation in air at the working temperature range of 550-850°C. However, to protect the alloy from continued oxidation, the alloy should develop a thin, dense, adhesive scale during the service life of the cell. Furthermore, this thin oxide layer should have adequate electrical conductivity to serve as electrical leads for the cell. Therefore, if an alloy develops a thin, dense oxide scale (such as alumina), if the conductivity of such an oxide is low then that alloy may not meet the requirements.

Most of the structural alloys for service at temperatures >550°C contain chromium. One of the issues with chromium-containing alloys is that the Cr_2O_3 scale (which normally forms in oxidizing environments) could undergo further oxidation to CrO_3,[20] which will vaporize at the working temperature. Steam in the environment exacerbates the formation of $CrO_2(OH)_2$. Alloys will be further oxidized after CrO_3 vaporizes. The CrO_3 vapor may react with other components of the cell such as solid state electrodes.[21,22] The electrochemical reduction of CrO_3 at cathode/electrolyte/gas phase boundary can lead to polarization losses.[23]

Interactions at elevated temperatures between the chromia-forming alloys with perovskite electrodes of types $(La,Sr)MnO_3$ and $(La,Sr)CoO_3$ may also degrade the electrodes. A significant transport of chromium from alloys to electrodes has been reported.[22] This transport can occur via solid state diffusion as well as via volatile chromium oxides. A thick spinel layer forms at the interface of electrodes and alloys leading to degradation of fuel cell performance.[21] To resolve this problem, there is a need to apply a coating that forms only harmless products by reaction with chromia without much reduction in the interface electrical conductivity.

Metallic alloys can undergo carburization in environments that contain hydrocarbons, especially in high concentrations. If the fuel gas is methane, carbon deposition, based on thermodynamics of gas phase reactions, can be expected in the temperature 550-850°C. The deposition of carbon may block the gas flow channels during long-term service and also may lead to corrosion of the metallic interconnect. All structural Fe-, Ni-, and Co-base alloys can undergo carburization and/or metal dusting at temperatures in the range of 350-1000°C, the extent of attack depending on the alloy composition, gas chemistry, temperature, and exposure time.[16-19]

This report addresses five topics of interest for the development of metallic interconnects with adequate performance in fuel cells for long service life. The research conducted over the years and the conclusions reached can be used to identify additional areas of research on materials for improved performance of components, especially metallic interconnects, in the complex fuel cell environments. This report address research conducted in the following areas:

1. Measurement of Area Specific Electrical Resistivity
2. Performance of Alloy 446 in Dual Gas Environments
3. Performance of Ferritic and Austenitic Alloys in Fuel-gas Environment
4. Approach to reduce the Area Resistance of Metallic Interconnect
5. Reduction of Electrical Resistivity of Alumina Scales on Metallic Interconnect.

2. MEASUREMENT OF AREA SPECIFIC ELECTRICAL RESISTIVITY

In high-temperature environments, chromium-containing alloys form a continuous chromium oxide scale, which acts as a rate-determining solid-state diffusion barrier between the environment and the alloy substrate. Therefore, chromium oxide is one of several important scales that can provide adequate corrosion resistance for metallic alloys. From the fuel cell application of Cr-containing alloys, it is essential that the chromia scale on the alloy surface possess low resistivity (high conductivity) during the service life of the fuel cell. Extensive work has been conducted to measure the electrical conductivity of thermally grown chromium oxide scale as a function of temperature and oxygen partial pressure in the exposure environment and to evaluate the transport mechanisms in the oxide.

The gas-tight electrochemical cell used for conductivity measurements with varying pO_2 is shown in Fig. 3. The ends of the cell consist of two identical yttria-stabilized zirconia (YSZ) discs. The top disc serves as an oxygen sensor and the bottom disc is primarily used an oxygen pump. Both YSZ discs were painted with platinum paste on the outer faces and on those parts of the inner faces that were to be exposed to the gas environment in the cell. These platinum electrodes were carried through several heating steps in air, with a final firing overnight at 980°C. The walls of the cell consist of seven 12.7 mm diameter high-purity alumina rings that are separated

from each other and the YSZ discs by thin Pyrex glass rings. The alumina rings serve as electrical insulators at high temperatures. Thin platinum wires were used as electrical leads. The entire assembly was placed in a resistance-heated furnace and spring force was applied from above. A 3 vol.% O_2-Ar gas mixture was flowed through the system during heating to a temperature of 1000°C. During heating, the Pyrex (which has a softening temperature of 820°C) melted and created a gas tight seal.

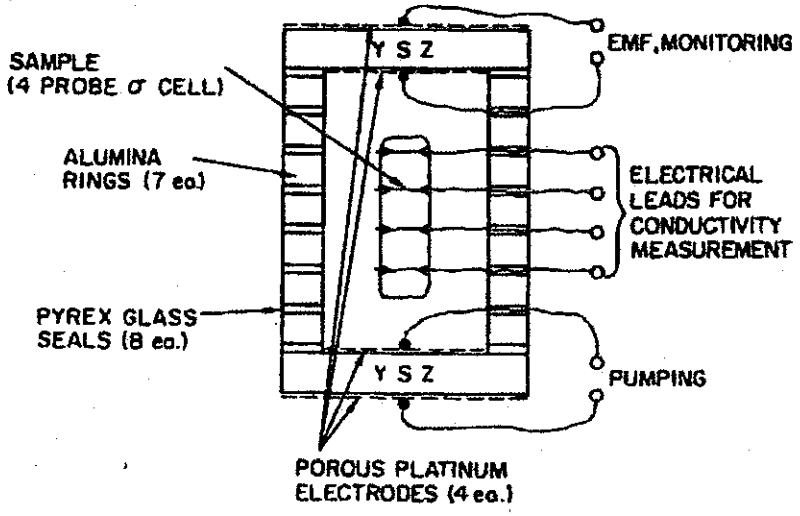

Figure 3. Cross-sectional view of gas-tight electrochemical cell containing standard four-probe conductivity sample.

Figure 4 shows a schematic of the specimen assembly used for conductivity measurements as a function of pO_2. A window ≈25 x 50 mm in size was cut near the bottom of an alumina tube with an outer diameter of 38 mm and a length of 350 mm, and the gas tight cell was inserted through the window. The tube was then sealed to the stainless steel head with high-temperature ceramic cement. An alumina 2-holer containing a thermocouple was then inserted into a 12.7 mm diameter alumina tube, which in turn was inserted into the 38 mm diameter tube so that the lower ends of both the 2-holer and 12.7 mm tube rested on the cell. A spring loading fixture was added at the top of the assembly to compress the cell stack by pushing down on the 2-holer. Finally, the outer tube was inserted into a quartz tube, 45 mm in diameter and 360 mm in length, which was secured with an O-ring fixture.

Fully oxidizing thin foils of pure chromium into chromium oxide and using them in a four-probe conductivity measurement system were the approaches used to determine the electrical conductivity of chromium oxide (see Fig. 5). Platinum wires, 125-μm thick, were wrapped around and spot-welded onto the specimens to serve as electrical leads. The electrical conductivity of the oxide samples was measured as a function of temperature and pO_2. Flowing either pure gases or mixtures that included CO, CO_2, N_2, O_2, H_2, H_2O, and CH_4 controlled the pO_2 values in the test environment. In the gas tight cell, air was used as the reference gas, and pO_2 in the chamber was maintained by pumping oxygen in/out with a dc current in the range of 1-600 μA.

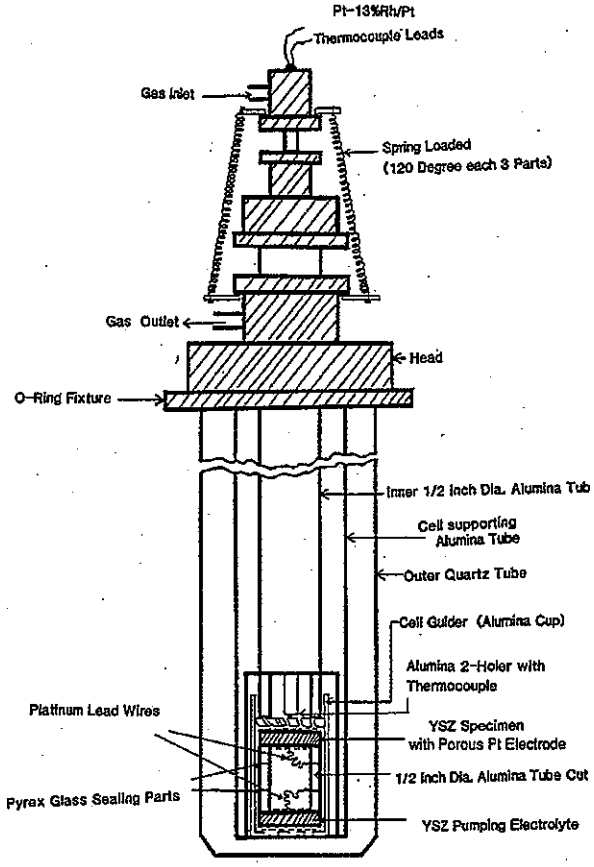

Figure 4. Schematic of apparatus used for four-probe electrical conductivity measurements at varying pO_2 levels, with sample in gas-tight cell.

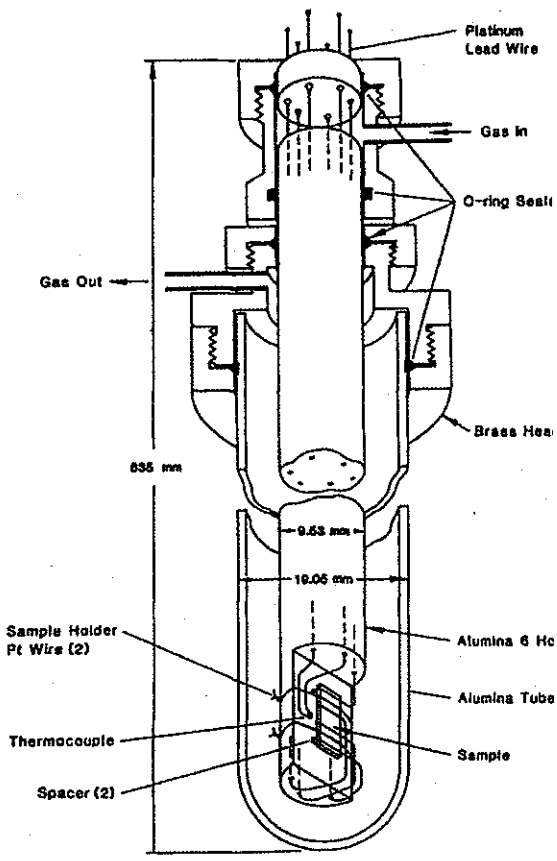

Figure 5. Schematic of apparatus used for four-probe electrical conductivity measurements at constant pO_2.

Figure 6 shows electrical conductivity data as a function of temperature and oxygen partial pressure for thermally grown chromium oxide scale measured by four-probe method in a gas-tight cell. The data indicate predominantly p-type behavior for the chromium oxide over the temperature range fro 577-1088°C and the pO_2 range from air to that corresponding to Cr/Cr_2O_3 equilibrium. To validate the data obtained with the gas-tight cell, experiments were also conducted with an open cell in an air environment; the results (see Fig. 7, open circles) are in excellent agreement with those obtained with a gas-tight cell (closed circles).

The conductivity data indicate that at ≈550°C, the values can range from 3×10^{-4} to 1.8×10^{-3} $\Omega^{-1}\cdot cm^{-1}$ as the pO_2 increases from 10^{-30} atm to 0.21 atm (air). At a temperature of 850°C, the corresponding values are 1.8×10^{-3} and 0.01 $\Omega^{-1}\cdot cm^{-1}$, respectively. Additional details on the defect structure, concentration, and mobility and their correlation with Cr oxidation characteristics can be obtained from an earlier publication.[24]

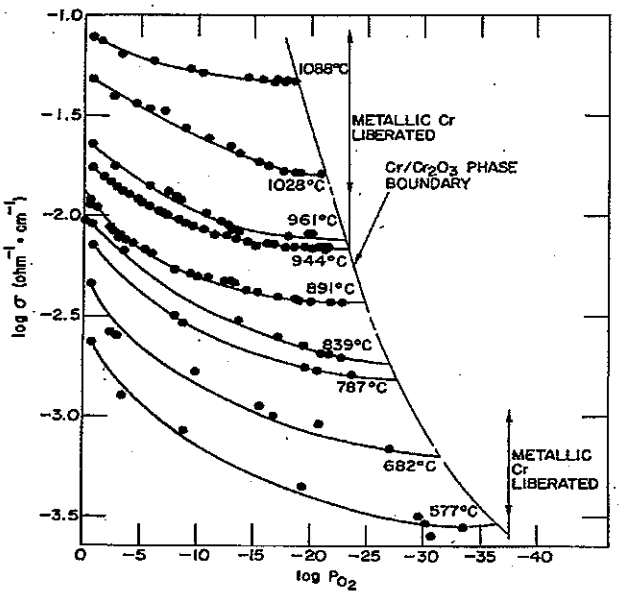

Figure 6. PO_2 dependence of electrical conductivity of a thermally grown chromium oxide scale measured in a gas-tight cell.

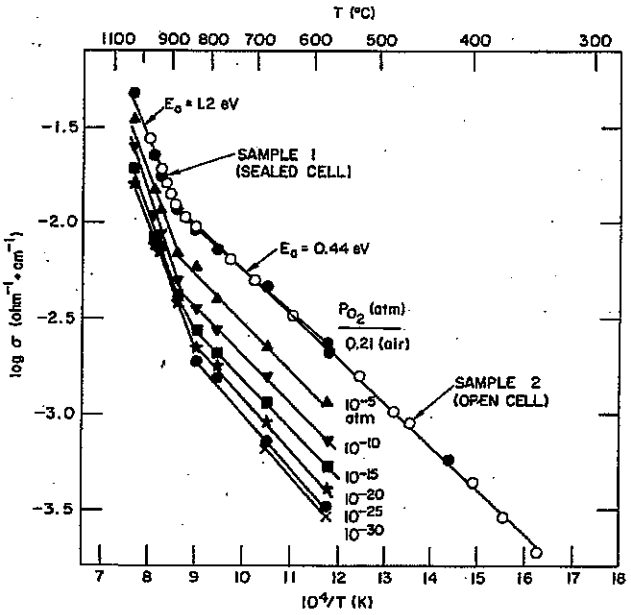

Figure 7. Temperature dependence of electrical conductivity of a thermally grown chromium oxide scale.

3. EXPERIMENTS IN DUAL GAS ENVIRONMENTS

To protect metallic interconnects from oxidation and carburization, the selected alloy has to develop a robust, slow-growing oxide scale with adequate electrical conductivity for electric current transport. Different alloys develop oxide scales with varying composition and microstructures, which can exhibit different capability to resist corrosion in a fuel cell environment. The electrical conductivity of oxide scales is also strongly dependent on the composition of the phases present in the scale. Generally, conductivity increases dramatically if mixed valence ions are present in oxides. For example, the conductivity of $Mn_{(1+x)}Cr_{(2-x)}O_4$ increases from 5.1×10^{-4} $\Omega^{-1} \cdot cm^{-1}$ for x = 0 to

0.3 $\Omega^{-1}\cdot cm^{-1}$ for x = 1 at 800°C,[25] when the oxidation state of Mn changes from +2 to +2.5. Therefore, it is necessary to evaluate the effects that the composition and oxidation state of ions in oxide scale on the electrical conductivity. The synchrotron X-ray near-edge absorption spectrum in Advanced Photon Source (APS) in Argonne National Laboratory provides an excellent method to study the oxidation state of ions in oxides. Sublayer structures in the oxide scale are often observed on the surface of alloys, and knowing the stability of their chemical composition, chemical state, and the crystallographic phase are of interest for fuel cell applications. However, the conventional X-ray diffraction (XRD) techniques are inadequate to determine the phases and the compositions and structures of each submicrometer thick sublayer, because the regular X-ray beam sizes are too large. The nanoprobe capability at the Argonne APS provides an opportunity to evaluate the local phase composition at oxide scale. We have used X-ray nanobeam to characterize the scale on the surface of Alloy 446 after exposure to air/hydrogen dual atmosphere at a wide range of temperatures and the results are presented in this section.

Alloy 446, a ferritic steel with a composition (in weight percent) of Cr 26.7, Ni 0.3, Mn 0.7, Si 0.5, and Fe balance, was selected for the study in dual atmospheres. Figure 8 shows a macrophotograph of alloy 446 tube of ≈33 mm o.d. used in our experiment. One end of the tube was sealed by welding a plug, and the other end was connected to two small diameter tubes that were used to deliver hydrogen to the inside of the alloy 446 tube. Six thermocouples were spot-welded onto the tube surface to measure the temperatures at different locations, which enabled us to evaluate the performance the alloy at several temperatures in one experiment. Two tubes were exposed for 1,030 h in a resistance-heated furnace with a center temperature of 850°C. One tube was tested in a dual atmosphere with wet hydrogen (2.3 vol.% H_2O) inside the tube, and air outside the tube. The other tube was tested with air both inside and outside of the tube in order to compare the effect of hydrogen on the growth of oxide scale. The tubes were cut into six pieces at the locations where thermal couples were attached (see Fig. 8), for post-exposure examination.

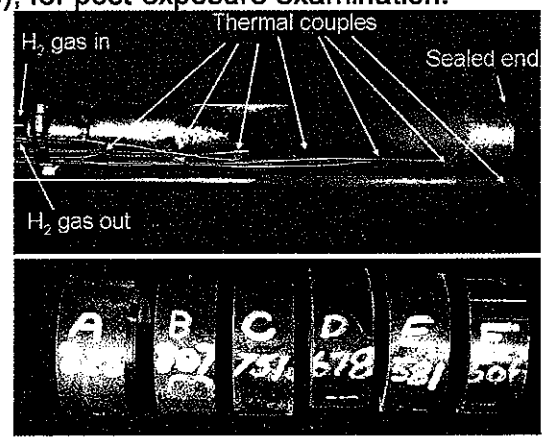

Figure 8. Tube of Alloy 446 after exposure in dual environment for 1030 h. The tube was cut into six pieces for analysis after exposure. The temperature of each piece was measured by a thermocouple that was welded to the piece.

All samples were ultrasonically cleaned in acetone. Standard metallographic techniques were employed to prepare the cross section mounts, which were used in scanning electron microscope (SEM) analysis. The distribution of the main constituent

elements (nickel, chromium, iron, and manganese) along with oxygen within the near-surface regions of the alloy was analyzed by energy dispersive X-ray spectroscopy (EDX) using a Hitachi S-4700-II scanning electron microscope. The cross-sectional samples were etched with 5% HNO_3 in methanol solution at 3V for ≈20 s after completion of EDX analysis to obtain better SEM images of the specimens.

Experiments were performed at the 2ID-D beamline of the APS at Argonne National Laboratory. Using zone plate diffraction optics, the X-ray nanoprobe in the experimental station produces a monochromatic X-ray beam of size 200 nm with a photon flux of 5 x 10^9 photons/s with an X-ray energy bandwidth (dE/E) of 0.01%. The position of the zone plate along the beam was adjusted so that the minimum spot size was obtained at the surface of the specimen. Figure 9 shows the scattering and data acquisition geometry for the synchrotron radiation experiments. When the focused beam was on the region of interest on the specimen, the scattering intensity in a section of reciprocal space was captured by a flat, two-dimensional detector (CCD camera). Samples for the synchrotron radiation experiments were prepared in a manner similar to that used for the cross-sectional analysis in scanning electron microscopy. The beam energy was 8.5 keV, and the CCD exposure time was 60 s for each spot in the scan. The position of the oxide-metal interface was determined by monitoring the Fe-fluorescence counts as the sample was translated across the beam.

The area resistivity of oxide scale on surface of alloys was measured by a four probe method.[24] Platinum paste was applied to the sample surface, and then platinum gauze was placed on top of the paste as current leads. Samples were set in a device that was described in a earlier paper.[24] The furnace temperature was controlled by a Eurotherm 2416 to increase or decrease at a rate of 1°C/min. A Keithley 228A current source and a Keithley 2700 multimeter/data acquisition system were used to provide a constant current and to measure the resulting voltage across the sample, respectively.

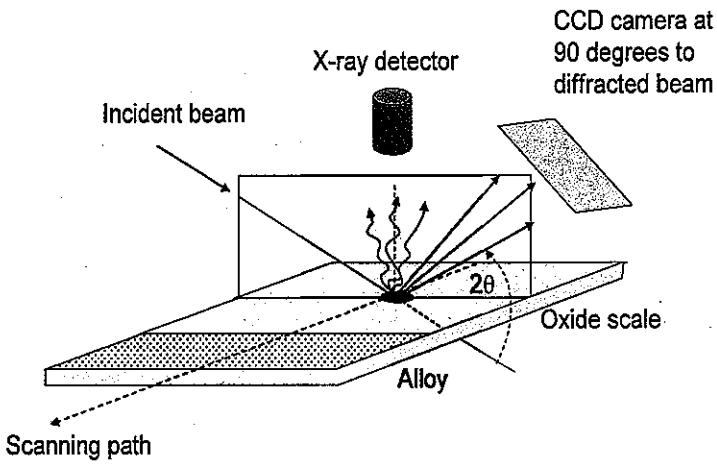

Figure 9. Schematic showing the geometry of data acquisition at the synchrotron beamline.

Experimental Results

The oxygen partial pressure in the H_2-2.3% H_2O environment is lower than that in air. For example at 800°C, the values were 2.4 x 10^{-20} and 0.21 atm for the hydrogen

side and air side, respectively. Therefore, the growth rates of oxide scale on the hydrogen side were much lower than that on the air side. Figure 10 shows SEM photomicrographs of cross sections of the alloy after oxidation at several temperatures in the dual environments. It is evident that the scales are much thinner in the hydrogen side when compared to those developed on the air side.

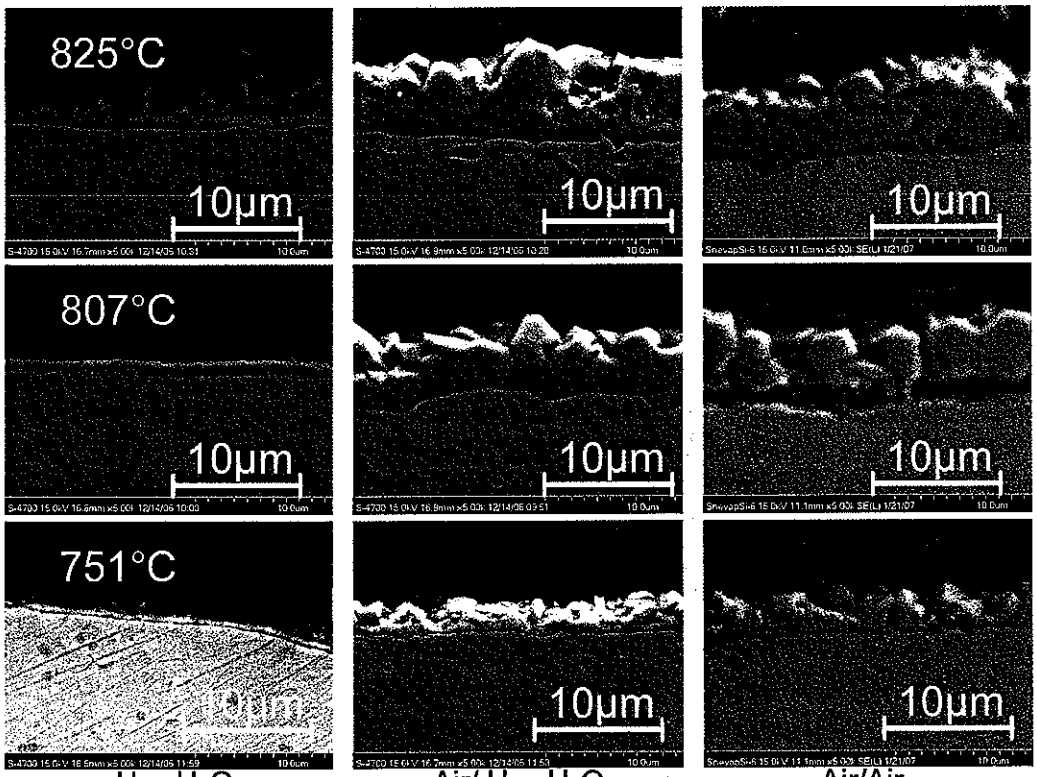

Figure 10. SEM cross section images of the alloy 446 tube tested at 825, 807, and 751°C in different environments.

The oxide scale on the moist hydrogen side was very thin (photographs in the left column in Fig. 10) when the tube was exposed in the dual atmosphere test whereas the oxide on the air side (photographs in the center column in Fig. 10) in the same test was much thicker, indicating that the oxygen pressure in the exposure environment has significant effect on the scale growth kinetics. The photographs in center and right columns in Fig. 10 show the air oxidation behavior of alloy 446 for the dual-gas environment and air only.

It was reported that in dual atmospheres, austenitic stainless steels exhibit anomalous corrosion performance under SOFC conditions and it was attributed to the presence of hydrogen in simulated fuel gas.[26] However, we did not observe such a mode of degradation for the Alloy 446 tube. The thickness of the oxide scales that developed on the air side in the dual atmosphere experiment and when the tube was exposed to air on both sides is of similar magnitude, indicating that the presence of moist hydrogen inside the tube did not accelerate oxidation of the alloy on the air side.

The oxide scales on the surface of alloy 446 were analyzed by SEM energy dispersive X-ray spectroscopy mapping (see Fig. 11). Two layers were observed in the oxide scales on tubes exposed in the air side of the dual environment and in the air/air environment. The major elements detected in the outer layer were oxygen, chromium, and manganese, whereas the chromium content in the inner layer was higher (see Fig. 12). Although alloy 446 contains only 0.7 wt.% manganese, it diffuses rapidly to the outer layer. No significant amount of iron in the oxide scale was detected, although the alloy contained ≈72 wt.% iron. The composition of oxide scales on both the air side of the air/H_2 dual environment and the air/air atmosphere were similar.

Energy dispersive X-ray spectroscopy is not amenable to evaluating the phases in the oxide scale, although we can obtain elemental composition by EDX. Regular X-ray diffraction can analyze the phase composition, but the X-ray beam could not be focused on the oxide scale in the cross section because the spot of the X-ray beam is much larger than the thickness of the oxide scale. Therefore, an X-ray nanobeam was used to examine the oxide scale. The combination of high flux and small spot size enabled us to study spatially resolved crystallographic phases and chemical states of scales on the surface of alloy 446. Figure 13 shows that the outer layer of the oxide scale is primarily spinel, and the inner layer consists of a mixture of chromium oxide and spinel phase. This result is consistent with the EDX analysis shown in Fig. 11. The outer layer is $Mn_{1+x}Cr_{2-x}O_4$, because the EDX analysis indicates that the outer layer consists of Mn, Cr, and O. Manganese diffused fast and accumulated to the outer layer. The phase distribution along the depth of the oxide scale is shown in Fig. 14. The oxide scale at the hydrogen side primarily consists of spinel. Although a weak diffraction peak of Cr_2O_3 was observed in the oxide scale at the hydrogen side, it was too weak to see in Fig. 14. Iron oxide (hematite) was observed in the oxide scale on alloy 430, with a composition (in weight percent) of Cr 16.5, Mn 0.5, Si 0.5, Fe balance, when it was exposed to the air/H_2 dual environment.[26, 27] It was reported that the hydrogen transport to the air side assisted in the formation of the hematite phase (α-Fe_2O_3).[27] However, in the present study we did not observe Fe_2O_3 on alloy 446. The higher Cr content in alloy 446 may have suppressed the formation of Fe_2O_3. Yang also reported that Fe_2O_3 was not observed on E-brite,[27] with a composition (in weight percent) of Cr 28, Ni 0.5, Mn 0.4, Si 0.4, Fe balance. Therefore, a higher chromium concentration in alloy seems necessary to prevent the alloy degradation in the dual gas environment. The diffraction intensity of alloy increases dramatically near surface. This may be the result of the surface reaction leading metal oxidation and needs further study.

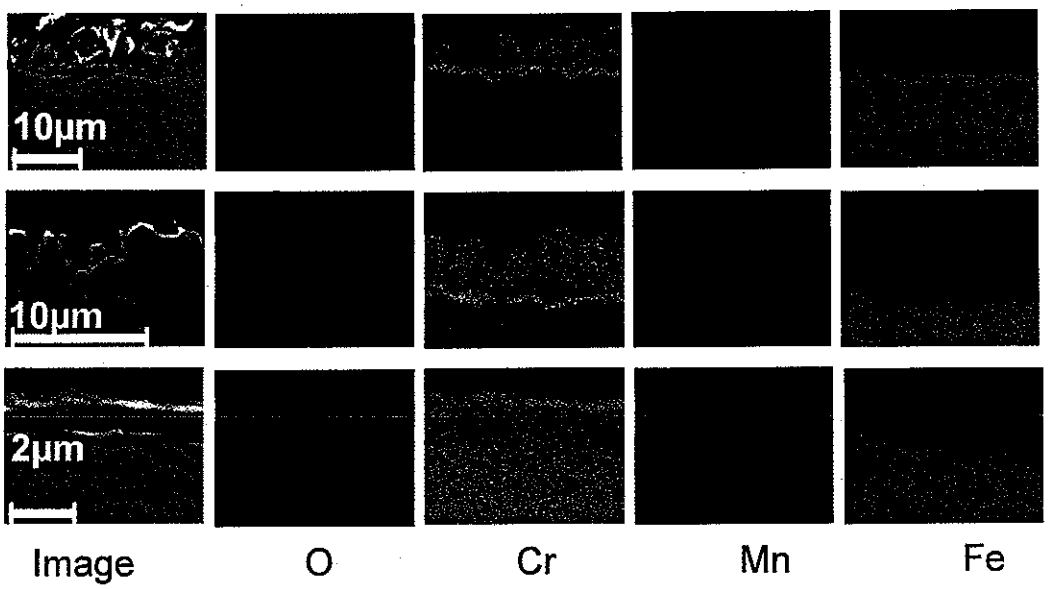

Figure 11. SEM energy-dispersive X-ray spectroscopy mappings of the cross sections of alloy 446. The outside of the alloy 446 tubes were exposed to air and the inside tubes have been exposed to 2.3%H_2O-H_2 at 807°C for 1,030 h.
Top row: Both surfaces of the tubes were exposed to air.
Middle row: The surface exposed to air with the other side exposed to 2.3%H_2O-H_2.
Bottom row: The surface exposed to 2.3% H_2O-H_2 with the other side exposed to air.

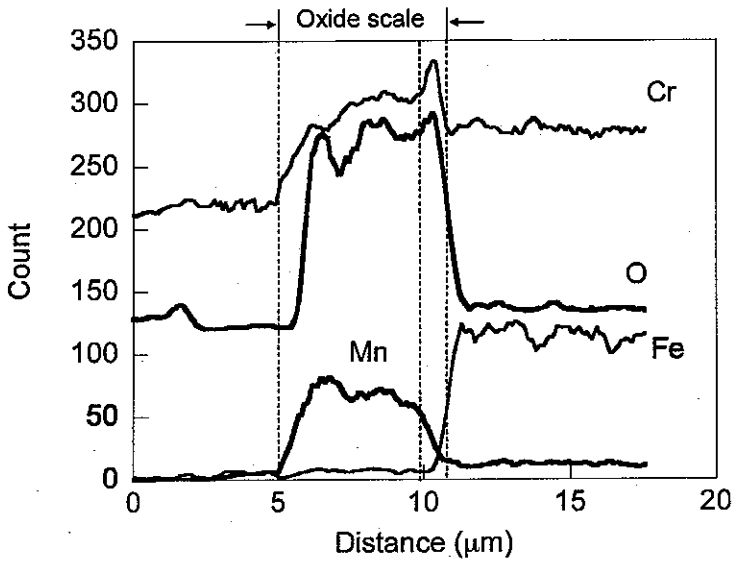

Figure 12. SEM energy-dispersive X-ray spectroscopy line scan through the cross section of the outside of the alloy 446 tube. The outside of the tube was exposed to air and the inside was exposed to 2.3% H_2O - H_2.

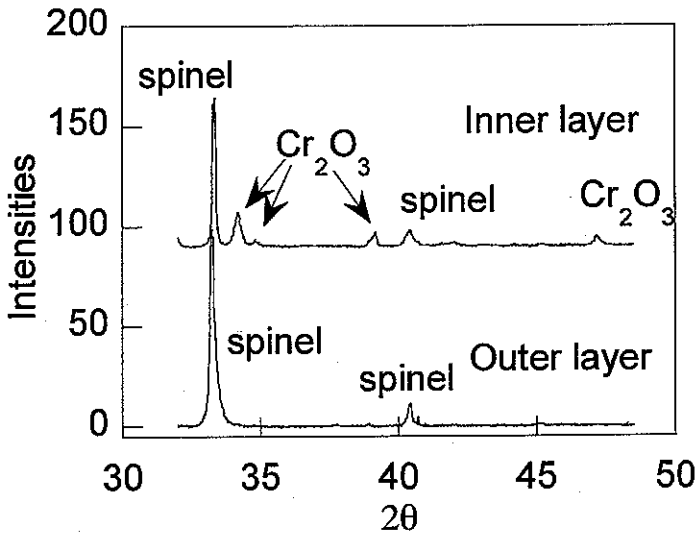

Figure 13. Nanobeam-X-ray diffraction of the oxide scale in the cross section of alloy 446 that was exposed to air for 1,030 h at 807°C while the inside of the tube was exposed to 2.3% H_2O - H_2.

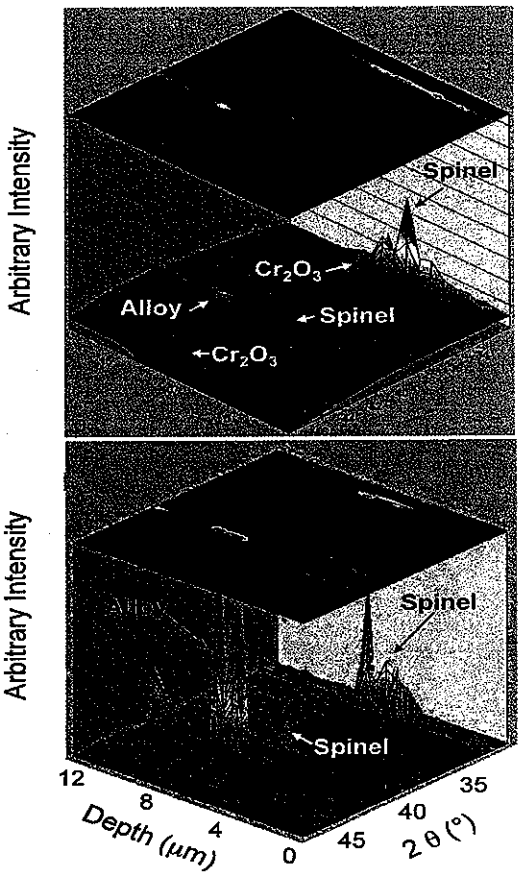

Figure 14. Nanobeam X-ray diffraction of the oxide scale in the cross section of alloy 446.
Top: air-exposed side;
Bottom: hydrogen-exposed side.

It is essential to evaluate the oxidation state of manganese in oxide scale because the electrical resistivity of the scale could significantly change, if a mixed valence state appeared in the oxide. Nanobeam X-ray near-edge absorption spectra

(XNEAS) were used to evaluate the oxidation state of manganese. Figure 15 shows the chemical shift of standard samples of $Mn^{2+}Cr_2O_4$, $Mn^{3+}{}_2O_3$, and $Mn^{4+}O_2$. Electrons need a higher energy to excite from 1S to 4P orbital when an oxidation state of Mn increases. When alloy 446 was exposed to hydrogen, the energy shift of manganese in the oxide scale was almost the same as +2 Mn in $Mn^{2+}Cr_2O_4$ standard. Thermochemical analysis also indicated that Mn^{3+} could be reduced to Mn^{2+} in a 2.3% H_2O-H_2 environment. Therefore, the oxidation state of manganese in the oxide scale is close to +2 when alloy 446 was exposed to hydrogen at 807°C. However, the energy shifts to between Mn^{2+} and Mn^{3+} when the alloy was exposed to air (see Fig. 15), which indicates that Mn is in a mixed valence state in the oxide scale on alloy 446 that has been exposed to air at 807°C.

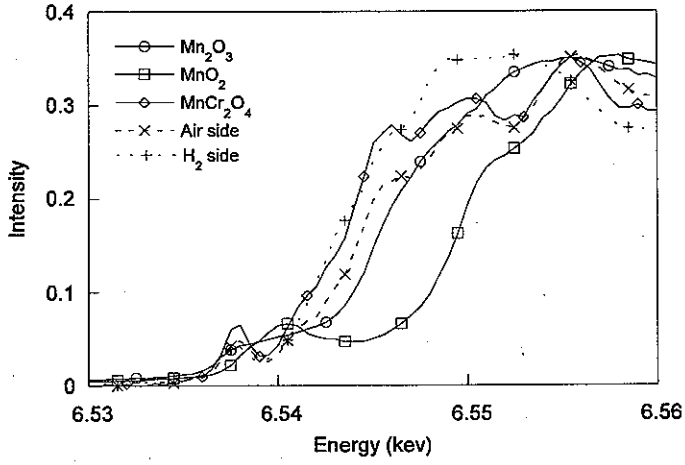

Figure 15. X-ray near-edge absorption spectra of Mn in standard samples of $MnCr_2O_4$, Mn_2O_3, MnO_2, and for the oxide scale on the surface of alloy 446 after exposure to hydrogen and air.

Figure 16(a) shows the area specific resistivity (ASR) values for the tube after 1,030 h exposure at several temperatures. ASR values are slightly higher on the surface of the specimen exposed to air than on the one exposed to moist hydrogen, primarily due to a larger oxide thickness in air than in hydrogen. Although the thickness of oxide scale decreases with a decrease in exposure temperature, the oxide thickness rather than temperature has a dramatic effect on ASR. For example, the ASR values of alloy 446 exposed to air at 678°C for 1,030 h are higher than that exposed at 751°C, because the resistivity of semiconductors dramatically increases at lower temperatures. Spinel is the major phase in oxide scale (see Fig. 13). Therefore, manganese valence in spinel should play a large role in the conductivity of the oxide scale. The resistivity of the oxide scales can be calculated by dividing the ASR value by the thickness of the scale. Since the thickness of the oxide scale on the air side are larger than that on the hydrogen side (see Fig. 10), the calculated resistivity of oxide scales on the air side is lower than that on the hydrogen side, as shown in Fig. 16(b). This observation can be explained by the presence of a mixed valence state of Mn in the scale on the air side with a lower resistivity than that on the hydrogen side, where the primary oxidation state of Mn is close to +2.

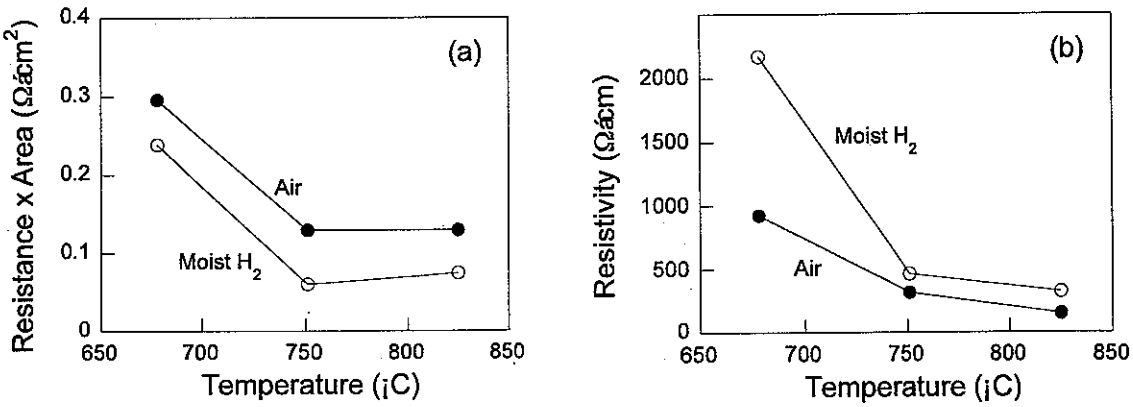

Figure 16. (a) Area specific resistance (ASR) for alloy 446 exposed to an air/H_2 dual gas environment and (b) resistivity of oxides, calculated by dividing the ASR values by the thickness of the scales.

In conclusion, alloy 446 was exposed to dual gases of air and 2.3% H_2O-H_2 at several temperatures in the range of 500-825°C. The synchrotron nanobeam X-ray diffraction analysis showed that oxide scale on the airside consisted of two layers. The outer layer was predominantly a spinel phase and the inner layer was a mixture of spinel and Cr_2O_3. The oxidation state of Mn in the spinel was between +2 and +3 when the alloy was exposed to air. The mixed valence state led to a lower resistivity for the oxide scale. However, the oxidation state of Mn in the spinel was close to 2 when the alloy was exposed to 2.3% H_2O-H_2 atmosphere.

4. PERFORMANCE OF METALLIC ALLOYS IN FUEL ENVIRONMENT

Metallic interconnect acts as a gas separator and distributor; therefore, it works in a dual-gas environment. The interconnect material is exposed to air on the cathode side and the alloy selected must be resistant to oxidation. On the anode (fuel) side, the gas environment will be dependent on the type of fuel selected for the application. For example, the fuel gas at the cell inlet can be a mixture of H_2 and CO (generated by external reforming or indirect internal reforming of natural gas) or a mixture of CH_4 and steam (for direct internal reforming), or pure H_2.

4.1 Gas Chemistry

The inlet gas in SOFC could be natural gas (mainly methane) or reformed gases consisting of a mixture of H_2, CO, CO_2, and H_2O. The composition of the flowing fuel gradually changes from high concentration of methane or H_2/CO mixture at the gas inlet to its oxidation products H_2O and CO_2, if the conversion is taken to completion. The H_2O content is low at the fuel cell inlet and gradually increases to high values at the outlet, depending on the degree of conversion. In addition, there can be a variation of ≈100°C or more in the cell temperature from the inlet to outlet. The combination of temperature variation and the change in gas chemistry can have significant effect on the development and maintenance of oxide scales that develop on the interconnect material

which in turn can affect the electrical conductivity of the oxide, especially over the long service life of the cell.

We performed thermodynamic calculations to characterize the fuel-cell environment as a function of temperature and for inlet gases of pure hydrogen or a gas mixture that arises from steam reforming of methane. The key parameters of interest from the metallic interconnect standpoint is the oxygen partial pressure and carbon activity (for the reformer gas) and their variation with temperature. The calculations were also made as a function of degree of conversion of the inlet as it transports through the cell from inlet to outlet. The characterized environments can be used to assess the surface gas-alloy interactions leading to oxidation and/or carburization of the interconnect materials.

Figure 17 shows the calculated results for oxygen partial pressure in the fuel cell environment when hydrogen is used as the fuel. We have used H_2-2.3% H_2O as the inlet gas to the cell and calculated the oxygen partial pressures as a function of the degree of conversion as the gas flows from the inlet to the outlet. It is evident that at any given temperature of the cell, the oxygen partial pressure increases as the conversion percent increases (i.e., a higher steam content in the gas). The information can also be used to establish the oxygen pressure at various temperatures, if the cell temperature varies from inlet to outlet. The results presented in Fig. 17 indicate that at a selected cell temperature of 800°C, the oxygen partial pressure can increase from 2.5 x 10^{-20} to 1.5 x 10^{-17} atm, as the steam content of the gas increases from 2.3 to 85%. On the other hand, as the cell temperature decreases from 800 to 600°C and for the hydrogen to steam conversion of 2.3 to 85%, the oxygen partial pressure can change from 2.5 x 10^{-20} to 3.2 x 10^{-23} atm.

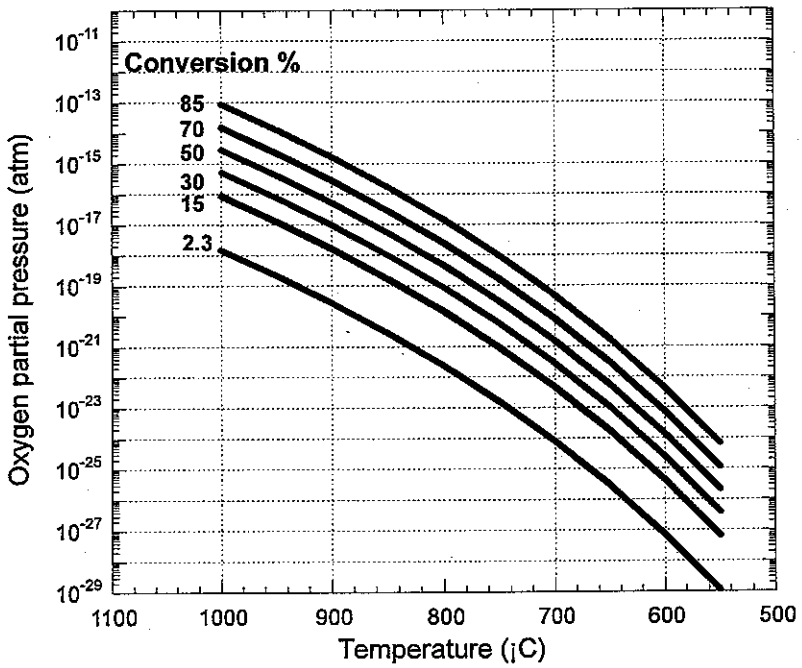

Figure 17. Calculated values for oxygen partial pressure as a function of temperature and degree of conversion for the cell inlet gas of pure hydrogen.

Figure 18 shows the calculated results for oxygen partial pressure in the fuel cell environment when a reformer gas mixture of 73.85% H_2-23.85% CO- 2.3% H_2O is used as the fuel. The results indicate that at a selected cell temperature of 800°C, the oxygen partial pressure can increase from 8.0×10^{-22} to 1.5×10^{-17} atm, as the conversion percent increases from 0 to 85. On the other hand, as the cell temperature decreases from 800 to 600°C and for the inlet gas conversion from 0 to 85%, the oxygen partial pressure can change from 8.0×10^{-22} to 3.2×10^{-23} atm.

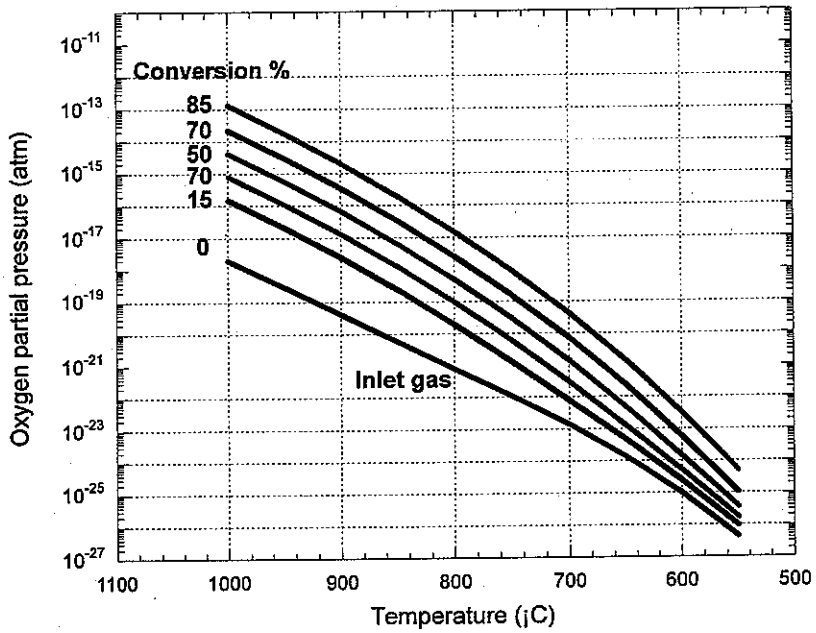

Figure 18. Calculated values for oxygen partial pressure as a function of temperature and degree of conversion for the cell inlet gas mixture consisting of 73.85% H_2-23.85% CO-2.3% H_2O.

When the reformer-based gas is used as the inlet gas for the fuel cell, the presence of CO and its conversion to CO_2 establishes a carbon activity which also needs consideration in the assessment of the corrosion performance of the interconnect material. Figure 19 shows the calculated results for carbon activity in the fuel cell environment when a reformer gas mixture of 73.85% H_2-23.85% CO- 2.3% H_2O is used as the fuel. The results indicate that at a selected cell temperature of 800°C, the carbon activity can decrease from an initial value 0f 1 (at the inlet) to 0.0008 at the outlet with 85% conversion. On the other hand, as the cell temperature decreases from 800 to 600°C and for the inlet gas conversion from 0 to 85%, the carbon activity can change from 1.0 to 0.026.

If coal derived gases are used as the feedstock in the SOFC, it is essential to consider not only the oxygen partial pressure and carbon activity in the gas mixture but also the sulfur (and may be chlorine) activity that may be present during the production of syngas from coal. The concentrations of sulfur and chlorine in the inlet gas will be strongly dependent on the method employed for the hot-gas cleanup as well the effectiveness of the cleanup procedure.

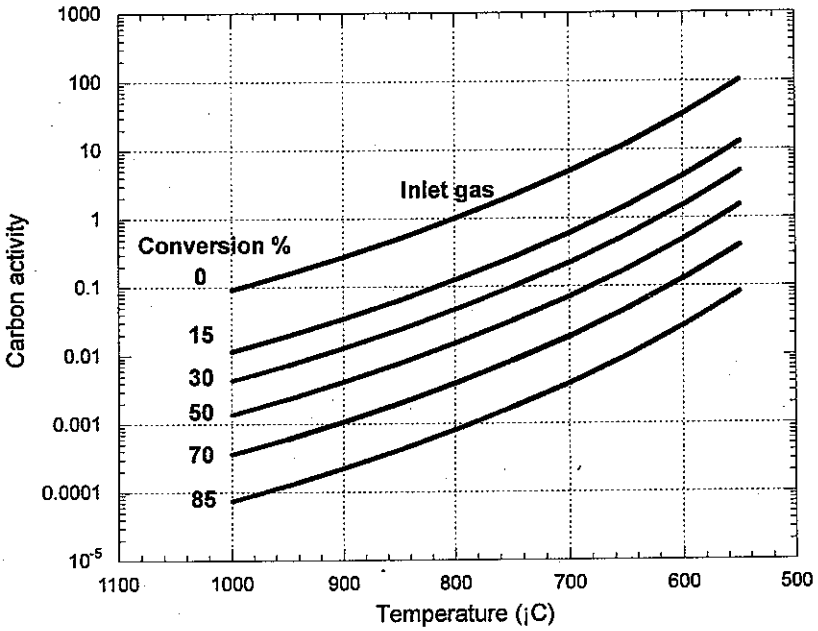

Figure 19. Calculated values for carbon activity as a function of temperature and degree of conversion for the cell inlet gas mixture consisting of 73.85% H_2-23.85% CO-2.3% H_2O.

4.2 Materials-Environment Interactions

In fuel cell environments that involve syngas or methane reformer-based gas containing oxygen and carbon, oxidation and carburization are the major modes of material degradation. Oxygen-carbon thermochemical diagrams can be used to examine the thermodynamic stability of various corrosion product phases that can form on a given alloy. The thermochemical diagrams depict the stability of the condensed phases for a given metal as functions of thermodynamic activities of oxygen and carbon in the gas mixture.

Figure 20 shows the iron-oxygen-carbon and chromium-oxygen-carbon thermochemical diagrams at 800°C superimposed on to common log pO_2 and carbon activity axes. In the figure, solid lines represent phase equilibrium boundaries for the pure metals and reaction products (oxides and carbides) at unit activity. Also shown in the figure are the pO_2 and a_C values for the reformer-based inlet gas (73.85% H_2-23.85% CO-2.3% H_2O) and at its conversion (in percent) of 15, 30, 50, 70, and 85. The calculations show that from the inlet to the outlet of the cell, the environment is such that the metallic interconnect (Fe- or Ni-base alloy) containing Cr would predominantly develop a mixture of oxides (such as chromia, spinel, and iron oxides) and carbides can form in the interior of the alloy, depending on the integrity of the surface of oxide and the extent of carbon transport through the oxide layer. Near the outlet of the fuel cell, the scale will be predominantly consist of Fe_3O_4 phase dictated by the high CO_2 and steam content in the gas.

Figure 21 shows the iron-oxygen-carbon and chromium-oxygen-carbon thermochemical diagrams at 650°C superimposed on to common log pO_2 and carbon activity axes. At this reduced temperature, the inlet gas has a much higher carbon activity which can lead to carburization (and possible deposit of carbon) of the alloy. However, at 15% conversion of the inlet gas, the carbon activity decreases significantly and the alloy may be subjected to oxidation coupled with internal carburization. The calculations clearly indicate the interplay between the initial gas composition, exposure temperature, and the degree of conversion of the feedstock in the cell and its effect on the scaling of the metallic alloy.

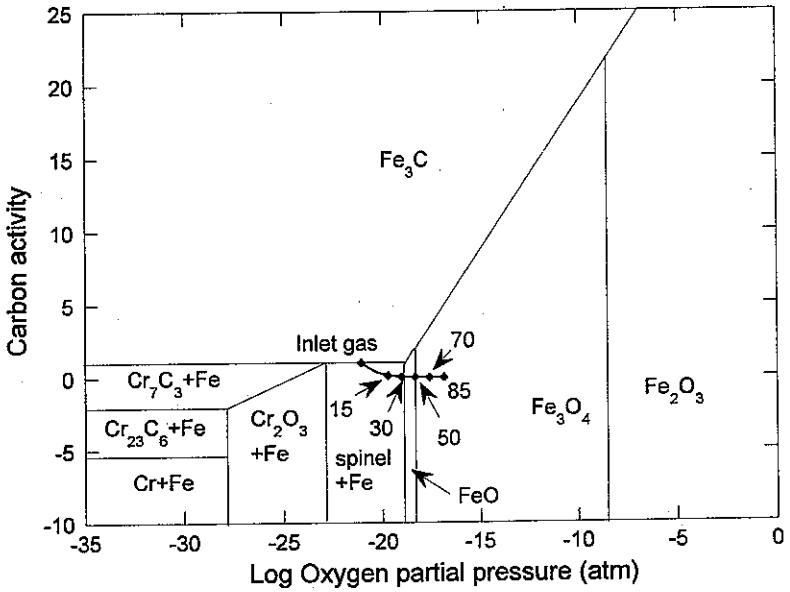

Figure 20. Oxygen-carbon thermochemical diagram depicting the stability of oxide and carbide phases in Fe- and Ni-base alloys at 800°C. Also shown are the pO_2 and a_C values for the reformer-based inlet gas and at its conversion (in percent) of 15, 30, 50, 70, and 85.

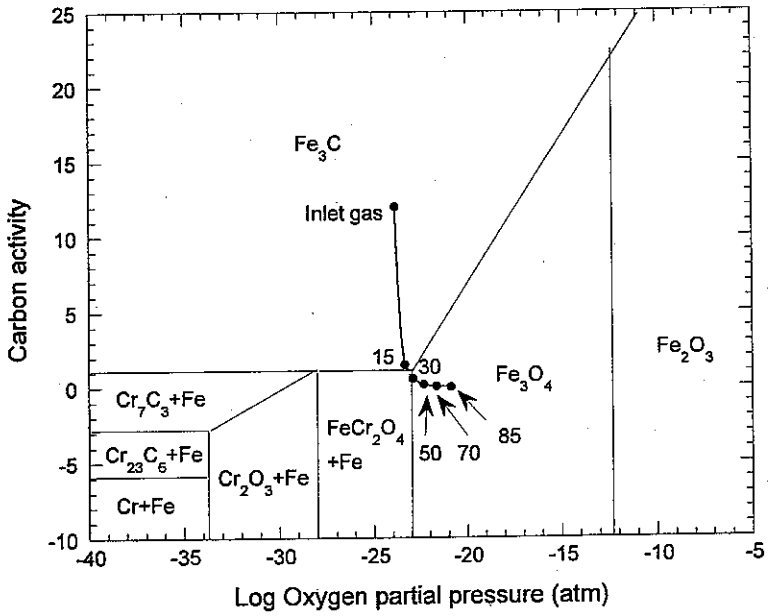

Figure 21. Oxygen-carbon thermochemical diagram depicting the stability of oxide and carbide phases in Fe- and Ni-base alloys at 650°C. Also shown are the pO_2 and a_C values for values for the reformer-based inlet gas and at conversion (in percent) of 15, 30, 50, 70, and 85.

4.3 Corrosion Performance of Commercial Alloys

During the past several years, a corrosion program funded by the U.S. Department of Energy (DOE) was conducted at Argonne National Laboratory, which involved research and development of materials, in accordance with the Program Plan for the Industrial Materials for the Future (IMF) subprogram. Consistent with the mission of the DOE Energy Efficiency and Renewable Energy (EERE) Industrial Technologies Program (OIT), the mission of the IMF subprogram is to lead a national effort to research, design, engineer, and test new and improved materials, as well as more profitable uses of existing materials, for the Industries of the Future (IOF). The test program had major objectives of establishing the mechanisms for corrosion degradation in reformer gas environments, characterizing the coking susceptibility of complex gas mixtures, and assessing the performance of materials exposed to such environments. Even though the tests were not conducted in direct support of solid oxide fuel cells, some of the test results and conclusions are applicable to understand the behavior of metallic interconnects and will be discussed below.

The Fe-base alloys included low-Cr ferritic steel (T22), intermediate-Cr ferritic steel (T91), and several high-Cr ferritic and austenitic steels and other alloys. Table 1 lists the nominal chemical compositions of the alloys selected for evaluation in the program. The Cr content of the latter alloys ranged between 17.3 and 28.0 wt.%. The Ni content of the high-Cr alloys ranged between 9.3 and 36.6 wt.%, except for ferritic alloys, which contained no/low nickel. Several of the Fe-base alloys contained a third element such as Al or Si, which has a high affinity for O. For example, MA956 and APMT contain 4.5 and 4.9 wt.% Al, respectively. Alloys 153MA, 253MA, and 353MA contain Si in a range of 1.3-1.6 wt.%.

Generally, the Ni-base alloys had a much more complex chemical composition since they contained Cr (in a range of 15.4-28.8 wt.%) and several other elements, such as, Mo (Alloys 617 and 625), Al (601, 617, 602CA, 214, and 693), and Si (45TM and HR 160). Further, several alloys contained Nb, W, and Co, which can also influence the oxidation behavior of the alloys and their resistance to carburization.

Tests were conducted in corrosion facilities that consisted of a horizontal, tubular, high-temperature furnace capable of operation up to 900°C. The reaction chamber, with gas inlet/outlet fittings, was fabricated from quartz and positioned within the furnace chamber. The ends of the reaction chamber had specially designed flanges with O-ring seals. A chromel-alumel thermocouple, inserted from one end of the reaction chamber, was used to monitor the specimen temperature. Specimens were suspended from quartz rods held on the top of a high-purity alumina boat. The specimens and the boat were positioned in the constant-temperature section of the reaction chamber. High-purity gases such as H_2, CO, CO_2, CH_4, and N_2 were procured and piped into the reaction chamber through flow meters to obtain the desired composition. In some experiments, H_2 gas was bubbled through a water bath to saturate the H_2 with water or water was pumped using a water pump and converted to steam prior to entering the

reaction chamber. Additional details on the experimental setup and operating procedures are presented in an earlier report.[19,28]

Table 1. Chemical composition (in wt.%) of alloys selected for evaluation.

Material	C	Cr	Ni	Mn	Si	Mo	Al	Fe	Other
Fe-base alloys									
T22	0.20	2.3	–	0.6	0.5	1.0	-	Bal	–
T91	0.08	8.6	0.1	0.5	0.4	1.0	-	Bal	N 0.05, Nb 0.07, V 0.2
153MA	0.05	18.4	9.5	0.6	1.4	0.2	-	Bal	N 0.15, Ce 0.04
253MA	0.09	20.9	10.9	0.6	1.6	0.3	-	Bal	N 0.19, Ce 0.04
353MA	0.05	24.4	34.7	1.4	1.3	0.1	-	Bal	N 0.18, V 0.06
310	0.03	25.5	19.5	1.7	0.7	-	-	Bal	-
800	0.08	20.1	31.7	1.0	0.2	0.3	0.4	Bal	Ti 0.31
803	0.08	25.6	36.6	0.9	0.7	0.2	0.5	34.6	Ti 0.6
321	0.04	17.3	10.3	1.2	0.4	-	-	Bal	Ti 0.4, N 0.01
APMT	0.04	21.7	-	0.1	0.6	2.8	4.9	Bal	-
4C54	0.17	26.7	0.3	0.7	0.5	-	-	Bal	N 0.19
330	0.05	19	35	1.5	1.3	-	-	Bal	
430	0.08	16.5	-	0.5	0.5	-	-	Bal	
EBrite	0.01	28	0.5	0.4	0.4	-	-	Bal	
RA85H	0.20	18.5	14.5	0.8	3.5	-	1.0	Bal	
Crofer	0.03	22	0.8	0.5	-	-	0.5	Bal	La 0.2, Ti 0.2, Cu 0.5
Ni-base alloys									
600	0.04	15.4	Bal	0.2	0.1	-	-	9.7	-
601	0.03	21.9	61.8	0.2	0.2	0.1	1.4	14.5	Ti 0.3, Nb 0.1
690	0.01	27.2	61.4	0.2	0.1	0.1	0.2	10.2	Ti 0.3
617	0.08	21.6	53.6	0.1	0.1	9.5	1.2	0.9	Co 12.5, Ti 0.3
625	0.05	21.5	Bal	0.3	0.3	9.0	0.2	2.5	Nb 3.7, Ti 0.2
602CA	0.19	25.1	62.6	0.1	0.1	-	2.3	9.3	Ti 0.13, Zr 0.19, Y 0.1
214	0.04	15.9	Bal	0.2	0.1	0.5	3.7	2.5	Zr 0.01, Y 0.006
230	0.11	21.7	60.4	0.5	0.4	1.4	0.3	1.2	W 14, La 0.015
45TM	0.08	27.4	46.4	0.4	2.7	-	-	26.7	RE 0.07
HR 160	0.05	28.0	Bal	0.5	2.8	0.1	0.2	4.0	Co 30.0
693	0.02	28.8	Bal	0.2	-	0.1	3.3	5.8	Nb 0.7, Ti 0.4, Zr 0.03
333	0.05	25	45	1.5	1.0	3	-	18	Co 3, W 3
HR120	0.05	25	37	0.7	0.6	2.5	0.1	33	Co 3, W 2.5, N 0.2

Tests were conducted in four different gas mixtures that are pertinent to SOFC. Table 2 lists the gas compositions and the calculated values for oxygen partial pressure and carbon activity (based on the reaction $CO+H_2=C+H_2O$) at 600 and 800°C. Gas 1 had the highest oxygen partial pressure and lowest carbon activity, primarily due high steam content. Gases 2, 3, and 4 had relatively high carbon content and relatively low oxygen partial pressure. Figures 22 and 24 show the calculated values of oxygen partial pressures and carbon activity as a function of temperature for the four gas mixtures listed in Table 2. These values are in a range similar to the reformer-based gas mixture with 0 to 50% conversion.

Table 2. Chemical composition (in mole %) and calculated oxygen partial pressures and carbon activity of gas mixtures used in the study

Gas	H_2	CO	CO_2	CH_4	H_2O	N_2	Oxygen partial pressure (atm)		Carbon activity	
							600°C	800°C	600°C	800°C
1	53.4	18.4	5.7	-	22.5	-	$3.7x10^{-25}$	$6.7x10^{-20}$	1.9	0.06
2	66.2	23	7.1	1.4	2.3	-	$1.1x10^{-25}$	$3.9x10^{-21}$	28.6	0.88
3	79.5	18.2	-	-	2.3	-	$6.3x10^{-26}$	$7.2x10^{-22}$	27.1	0.83
4	40.4	19.8	0.2	0.5	0.1	39.3	$3.0x10^{-26}$	$1.1x10^{-22}$	27.1	0.83

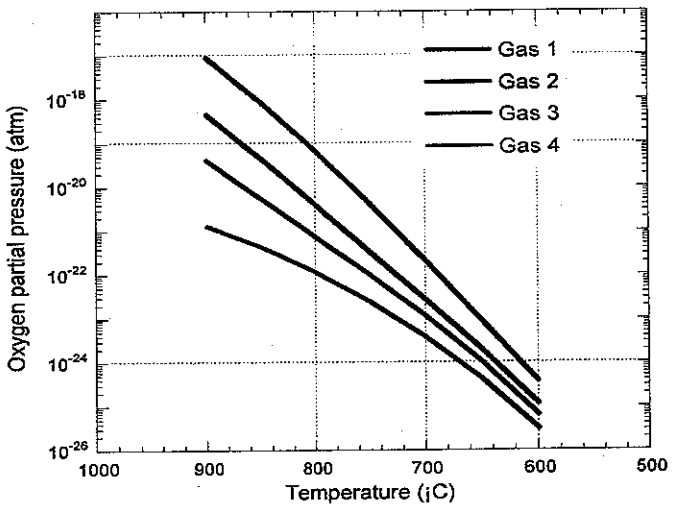

Figure 22. Calculated values for oxygen partial pressure as a function of temperature for four gas mixtures listed in Table 2.

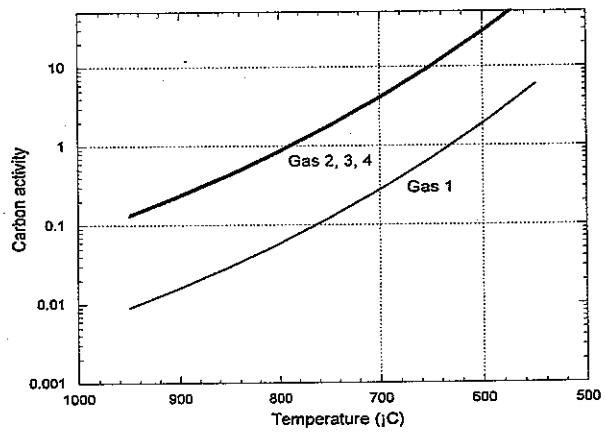

Figure 23. Calculated values for carbon activity as a function of temperature for four gas mixtures listed in Table 2.

Upon completion of the exposures, the specimens were cleaned of coke, if any, and weight change was determined. The microstructure of each sample was examined with a JSM-6400 scanning electron microscope. To study the metallographic cross section, the samples were electrolytically etched with 10% acetic acid at 10V for 30 sec. Raman spectra were excited with 60 mW of 476-nm radiation from a Kr-ion laser. The

incident beam impinged on the sample at an angle close to 45° from the normal. Scattered light was collected along the surface normal with an f/1.4 lens. The scattered light was analyzed with a triple Jobin-Yvon grating spectrometer and detected with a CCD detector from Princeton Instruments. All of our spectra were acquired in 300 sec at room temperature.

4.4 Effect of Alloy Composition on Corrosion Rate

The metal loss rates are given in Table 3 for the alloys exposed for 1,000 h to Gas 2 at 593°C. Several conclusions were reached. Low Cr alloys such as T22 and T91 lose weight rapidly. Increasing Cr content in alloy decreases the corrosion rate. Ni-base alloys performed better than Fe-base alloys. Nickel-base alloys were resistant to corrosion after 1,000 h exposure at 593°C.

Figure 24 shows metal dusting pits that formed in Alloy 321 and 800 after 1000 h in Gas 2. A pit with 380-μm deep was observed in Alloy 321 after 1,000 h. Oxide layers on the surface of Alloy 800 were observed by scanning electron microscopy (SEM). X-ray diffraction (XRD) of the layer showed major phases to be spinel and Cr_2O_3 (see Fig. 25). However, the oxide layer was not present in the pit area.

The most intense Raman bands from Cr_2O_3 and spinel are the peaks at 551 cm^{-1} and 670 cm^{-1}, respectively.[29] Raman spectra also showed Cr_2O_3 and $(Fe,Mn,Cr)_3O_4$ spinel phases in the area without pits (see Fig. 26), and no oxide in the pit area. This result indicates that the oxide layer protects alloys from continued corrosion. When the oxide layer is removed, the alloys are directly exposed to carburizing gas. Therefore, a dense, adhesive oxide layer is important to prevent an alloy from undergoing continued degradation.

Table 3. Weight loss data for alloys after exposure at 593°C for 1,000 h in Gas 2 (66.2% H_2-7.1% CO_2-23% CO-1.4% CH_4-2.3% H_2O)

Alloy	Mass loss (mg/cm^2 h)	Visual examination
T22	0.5	Heavy carbon deposit
T91	0.066	Pits
153MA	0	Clean surface
253MA	0	Clean surface
310	0	Clean surface
800	0.045	Pits
321	$3.8x10^{-3}$	Pits
600	0	Clean surface
601	0	Clean surface
690	0	Clean surface
617	0	Clean surface
214	0	Clean surface
602CA	0	Clean surface
230	0	Clean surface

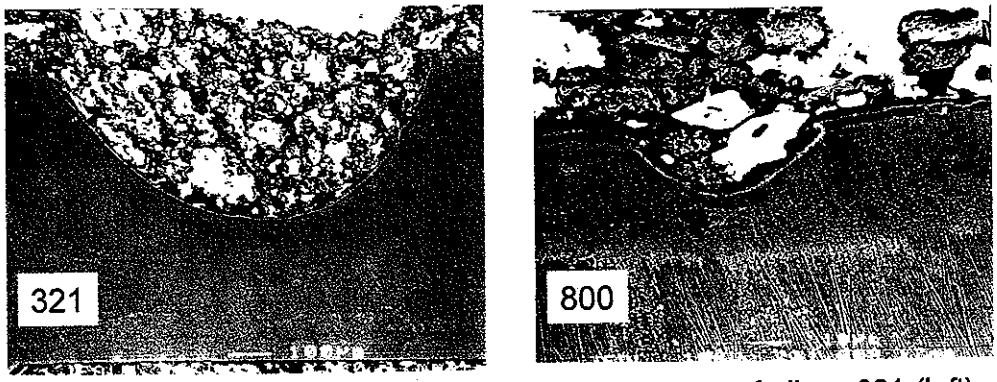

Figure 24. SEM micrograph of metallographic cross section of alloys 321 (left) and 800 (right) after exposure in Gas 2 (66.2% H_2-7.1% CO_2-23% CO-1.4%CH_4-2.3% H_2O) at 593°C for 1,000 h.

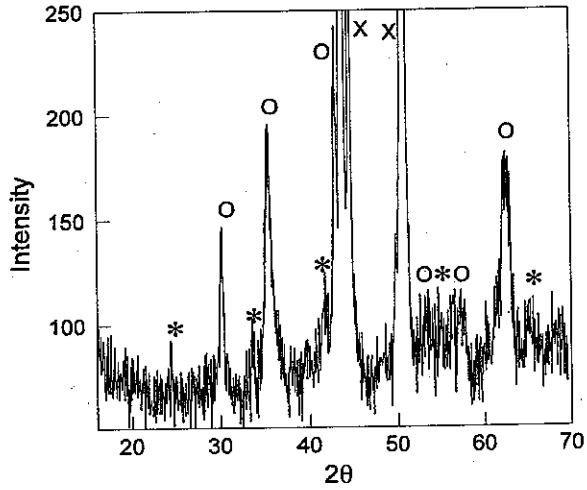

Figure 25. X-ray diffraction of oxide scale on the surface of Alloy 800 after exposure in Gas 2 (66.2% H_2-7.1% CO_2-23% CO-1.4%CH_4-2.3% H_2O) at 593°C for 1,000 h. *: Cr_2O_3; o: spinel; x: alloy substrate.

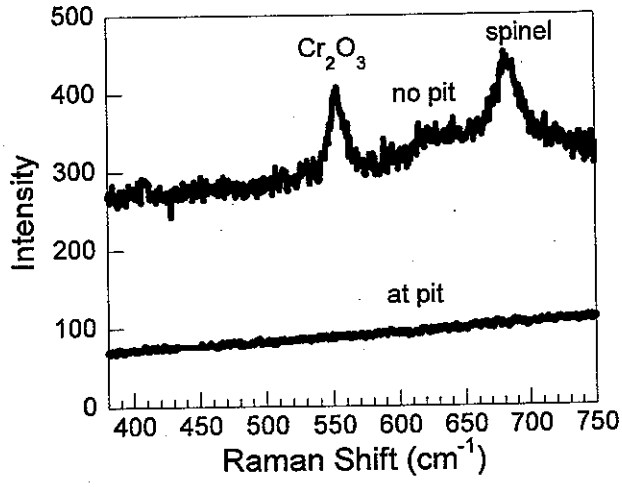

Figure 26. Raman spectra of Alloy 800 at pit and no-pit areas. Specimen was exposed to Gas 2 at 593°C, 1 atm for 1,000 h.

Figure 27 shows the Raman spectra (frequency range 350-750 cm^{-1}) for several Fe-base alloys with different Cr contents, after 1000-h exposure in Gas 2 at 593°C. The

Raman spectra in the frequency range 200-800 cm^{-1} clearly show that alloys with Cr >8.6 wt.% develop more protective oxide scales. The peaks at ≈550 and ≈680 cm^{-1} correspond to Cr_2O_3 and (Fe,Cr) oxide spinel, respectively. Lack of oxide scale on alloy T22 (which contained 2.3 wt.% Cr) led to severe attack during the 1000-h exposure in the same experiment. The Raman peak intensities of Cr_2O_3 increase with increasing Cr content in alloys and the degree of attack decreases with increasing Cr content in alloys. It is concluded that Cr_2O_3 (rather than the spinel) is a more desirable phase in the scale to protect alloys from continued corrosion.

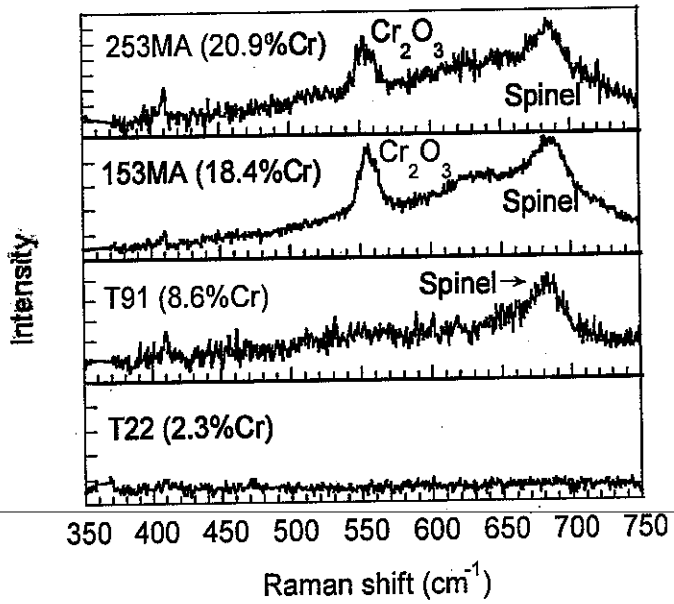

Figure 27. Raman spectra of Alloys T22, T91, 153MA, and 253MA after exposure in Gas 2 (66.2% H_2-7.1% CO_2-23% CO-1.4% CH_4-2.3% H_2O) at 593°C for 1,000 h.

Figures 28 and 29 show the difference in Raman spectra for two pairs of alloys: Alloys 253MA and 601, and Alloys 310 and 602CA. These alloys were exposed to Gas 1 at 593°C for 1000 h. The Cr contents in Alloys 253MA and 601 are similar. However, the Fe-base alloy 253MA has a much stronger spinel peak than that of the Ni-base alloy 601. Pits were observed on Alloy 253MA, but not on Alloy 601 after exposure under the same experimental conditions. The Cr contents in Alloy 310 and 602CA are also similar. Figure 29 shows the strong spinel peak for the Fe-base Alloy 310, but almost no such peak for the Ni-base Alloy 602CA. Pits were again observed only on Alloy 310, but not on Alloy 602CA. Less spinel in the oxide scale of Ni-base alloys may be a possible reason that the corrosion performance of Fe-base alloys is inferior to Ni-base alloys.

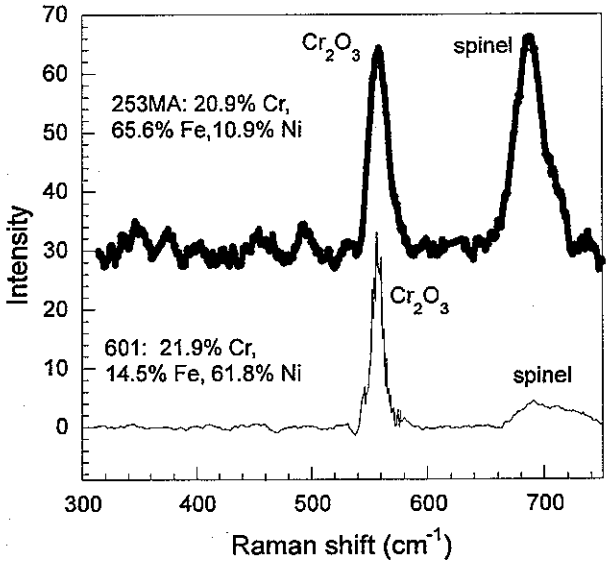

Figure 28. Raman spectra of Alloys 253MA and 601 after 1,000 h exposure in Gas 1 (53.4% H_2-18.4% CO-5.7% CO_2-22.5% H_2O) at 593°C for 1,000 h.

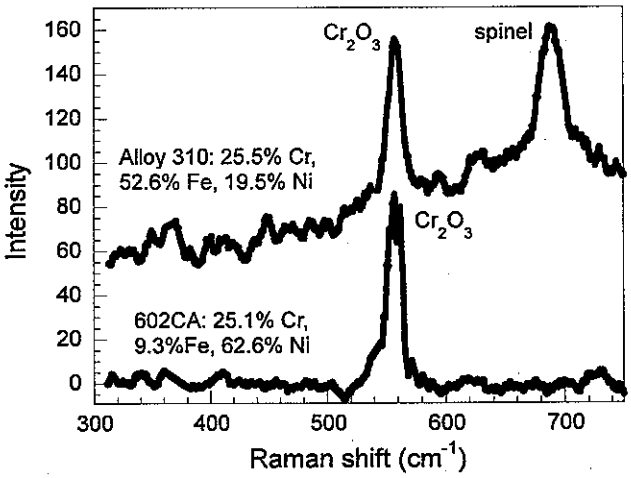

Figure 29. Raman spectra of Alloys 310 and 602CA after 1,000 h exposure in Gas 1 (53.4% H_2-18.4% CO-5.7% CO_2-22.5% H_2O) at 593°C for 1,000 h.

In contrast to austenitic alloys, ferritic alloys such as Alloys 446, MA956, and APMT were not attacked after exposure in Gas 3 at 593°C and 1 atm for 8,400 hours (see Fig. 30). High contents of chromium and aluminum may be responsible for their good performance in carburizing environment.

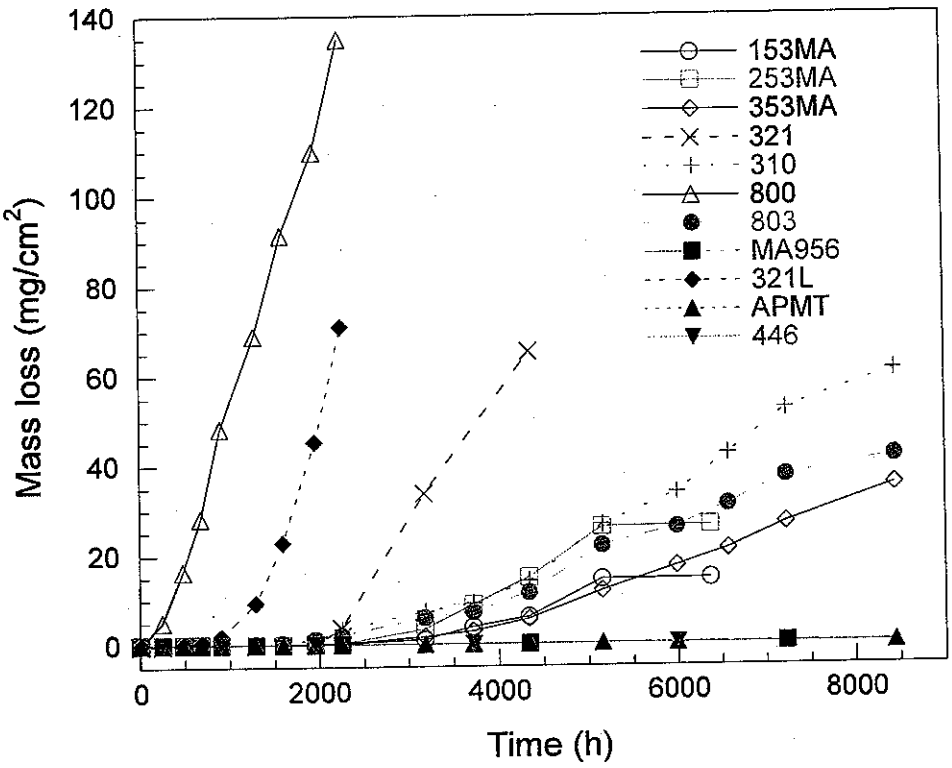

Figure 30. Weight loss of alloys exposed to Gas 3 (79.5% H_2-18.2% CO-2.3% H_2O) at 1 atm and 593°C.

However, ferritic alloys 430, Crofer, and Ebrite lost weight rapidly in Gas 4 at 1 atm and 593°C (Figs. 31a and 31b). Pit depth measurements made on several of the specimens showed deep pits on Crofer alloy (see Fig. 32). Figure 33 shows SEM cross section of a deep pit on Crofer alloy. We did not measure the pit depth of Alloy 430 because a pit has penetrated through the wall (thickness = 460 μm) within 960 h. Although the pits on Alloy 430 developed fast, the pit density was low. Therefore, the weight loss of this sample was not large (see Fig. 31). The pit density on Alloy 120 is high, which leads to rapid weight loss. Pit sizes on Alloy 120 were also large although the chromium content in Alloy 120 (25 wt.%) is high. Two layers were observed in the oxide scale at pit area on Alloy 120. However, a thin layer was observed at the non-pit area (Fig. 34). Similar microstructures were also observed for the oxide scales on Alloy Ebrite and 321 (Figs. 35 and 36). Alloy 446 and RA85H were not attacked and thin oxide scales were observed on their surfaces (Fig. 37).

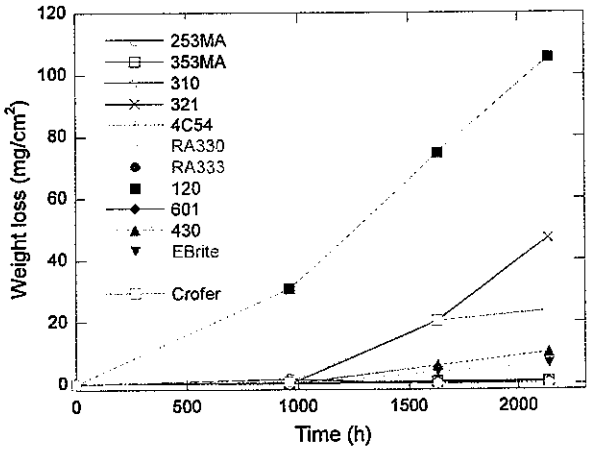

Figure 31a. Weight loss of commercial alloys that have been exposed to Gas 4 (40.4% H_2-19.8% CO-0.2% CO_2-0.5% CH_4-0.1% H_2O-39.3% N_2) at 593°C and 1atm.

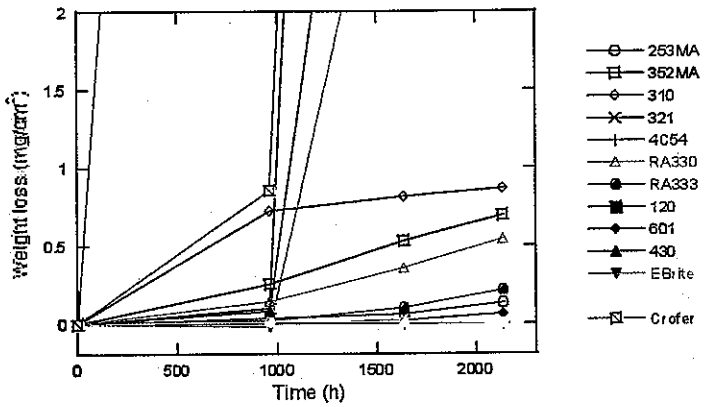

Figure 31b. Expanded view of weight loss of commercial alloys shown in Figure 31a.

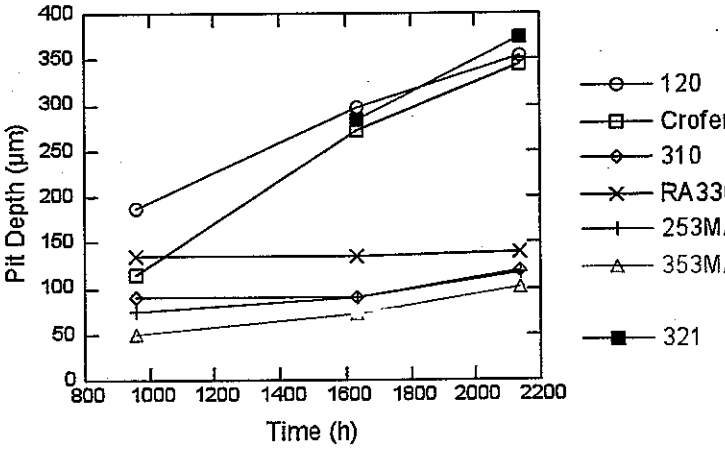

Figure 32. Pit depth data for alloys that were exposed to Gas 4 (40.4% H_2-19.8% CO-0.2% CO_2-0.5% CH_4-0.1% H2O-39.3% N_2) at 593°C and 1atm.

Figure 33. A corrosion pit on Crofer alloy after 2,136 h exposure in Gas 4 at 593°C and 1atm.

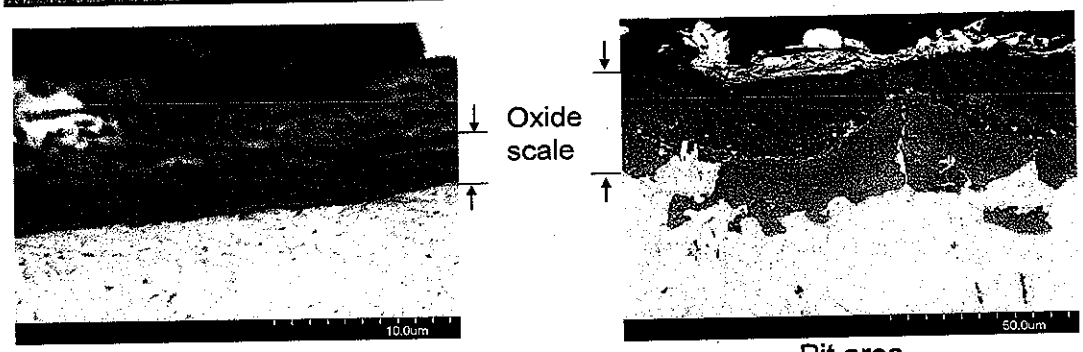

Non-pit area Pit area

Figure 34. SEM photomicrographs of cross section of Alloy HR120 at pit and non-pit areas.

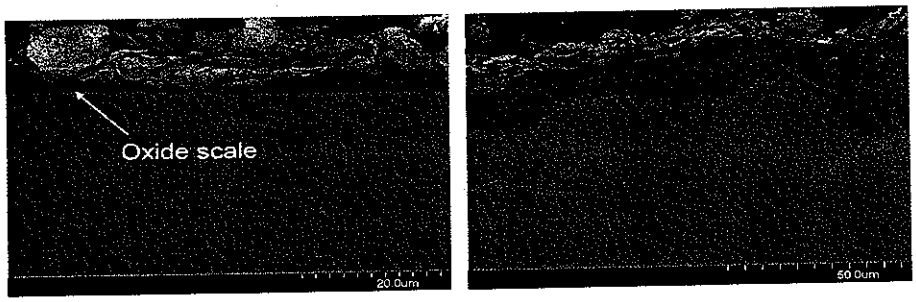

Non-pit area Pit area

Figure 35. SEM photomicrographs of cross section of Alloy Ebrite at pit and non-pit areas.

Non-pit area Start of attack Pit area

Figure 36. SEM photomicrographs of cross section of Alloy 321 at pit and non-pit areas.

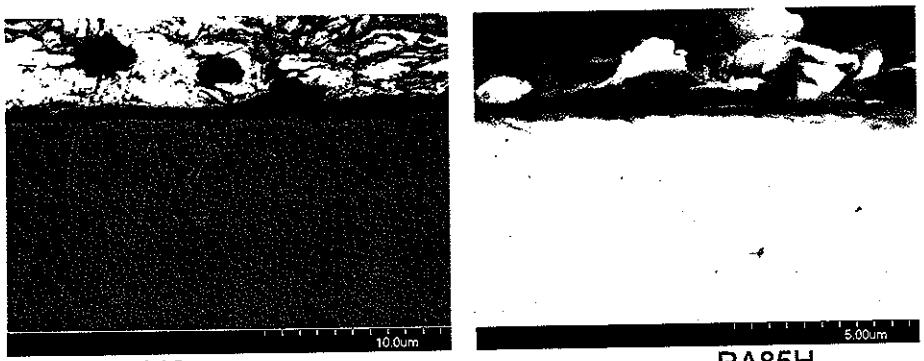

Figure 37. SEM photomicrographs of cross section of Alloy 446 and RA85H.

4.5 Effect of Temperature on Corrosion Rate

Two sets of alloys were exposed to Gas 4 at 1atm and 815 and 593°C. Only Alloy EBrite was attacked at 815°C after 5,716 h exposure as shown in Figure 38. However, the carbon activity increases at low temperature. Most alloys except Alloy 446 and RA85H were attacked after exposure to Gas 4 at 593°C and 1atm for 2,136 h (Fig. 39). High silicon content (3.5 wt.%) in Alloy RA85H may protect this alloy from corrosion. EBrite was corroded almost uniformly. The density of pits on Alloy 120 was high. Corrosion in Alloys 321 and Crofer initiated at specimen edges.

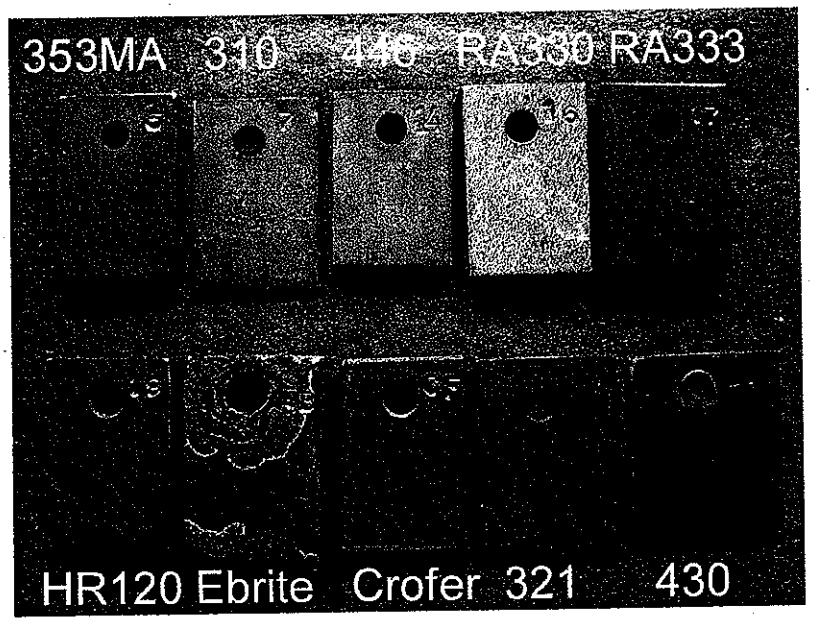

Figure 38. Macrophotograph alloys after 5,716 h exposure Gas 4 at 815°C, 1atm.

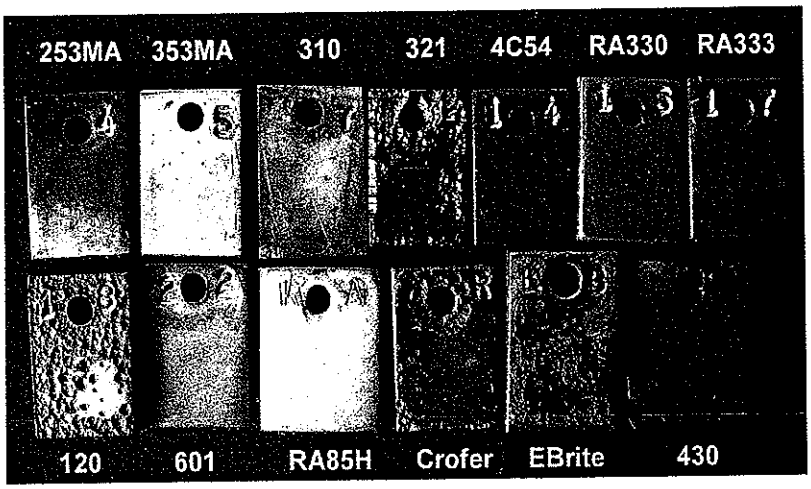

Figure 39. Macro-photograph of alloys after 2,136 h exposure to Gas 4 at 593°C, 1atm.

4.6 Effect of Gas Chemistry on Corrosion Rate

The metallic interconnects exposed to reformer-based gas mixtures can undergo corrosion depending on the gas chemistry and the exposure temperature. In particular, there may be a minimum value for the steam content of the gas for the metallic alloy to develop an oxide scale on the surface. In the absence of steam or below the minimum steam content, carbon activity in the gas could be high and carburization and/or metal dusting type reactions may dominate. Since gas composition in SOFC changes from low to high steam content from the inlet to the outlet of the cell, we compared the corrosion performance of alloys exposed to gas mixtures that contained 2.3 and 22.5% steam at 593°C. The steam content of Gas 2 is only one tenth of that of Gas 1, but the other constituents are similar for the two gases. The carbon activity of both gases are larger than 1 at 593°C. Figure 40 shows macrophotographs of specimens exposed in the two gas mixtures. Pits were observed in Alloy T91, 321, and 800 when exposed for 1,000 h to Gas 2 (low steam content). In contrast, no corrosion pits were observed in these alloys when exposed to Gas 1 (higher steam content) for the same period.

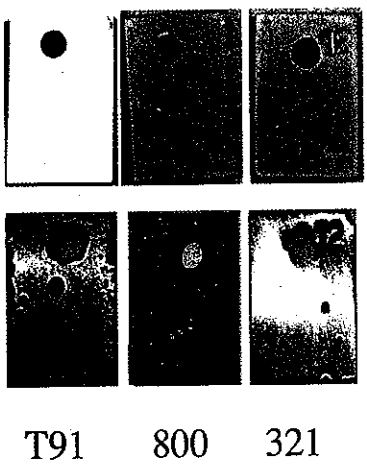

Figure 40. Macrophotographs of alloys after 1,000 h exposure to Gas mixtures 1 (high steam content) and 2 (low steam content) at 593°C.

4.7 Effect of System Pressure on Corrosion Rate

In the SOFC-gas turbine system, the fuel cell needs to operate at elevated pressure and the cell components need to perform adequately in the prevalent gas environments at elevated pressure. We have tested alloys at 15 atm and 593°C in Gas 1. Corrosion rates are sensitive to gas pressure for both Fe- and Ni-base alloys, since the gas phase reactions are strongly influenced by system pressure.

Figure 41 shows metal loss of four Fe-base alloys. The major phase in the oxide scale on Alloy 253MA was Cr_2O_3 when experiments were conducted at 1 atm. However, Cr_2O_3 was virtually absent when it was tested at 15 atm, and iron-chromium spinel was the predominant phase (Fig. 42). In contrast, Cr_2O_3 was still the major phase on the non-pit surface of Alloys 310, 800, and 321 after exposure in high-pressure environment. However, only spinel was observed at the pit regions of the specimens (Figs. 43 and 44). The corrosion behavior of Alloy 253MA was also different from that of Alloys 310, 800, and 321. The entire surface of Alloy 253MA was uniformly attacked by corrosion. However, Alloys 310, 800, and 321 were attacked only locally at pits.

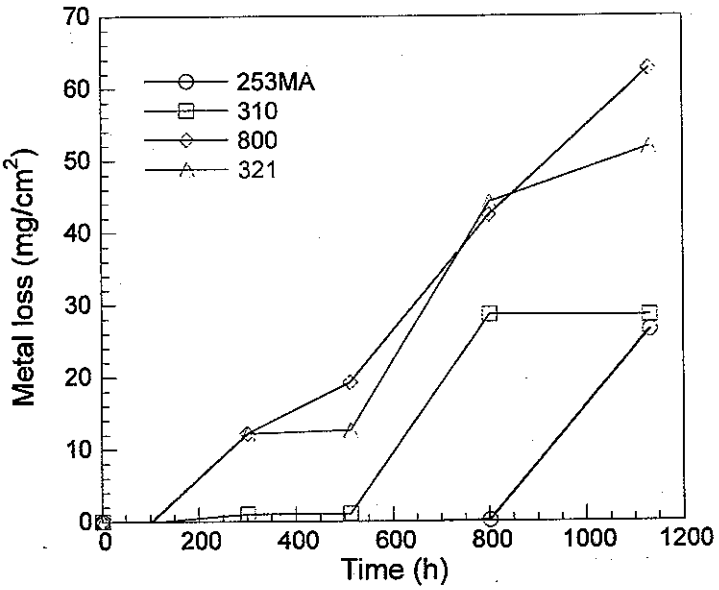

Figure 41. Weight loss data for Alloys 253MA, 310, 800, and 321 exposed to Gas 1 (53.4% H_2-18.4% CO-5.7% CO_2-22.5% H_2O) at 15 atm and 593°C.

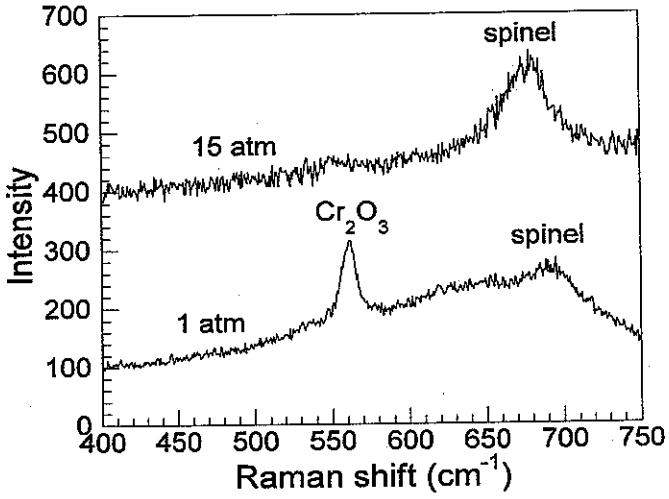

Figure 42. Raman spectra of Alloy 253MA tested at 1 and 15 atm in Gas 1.

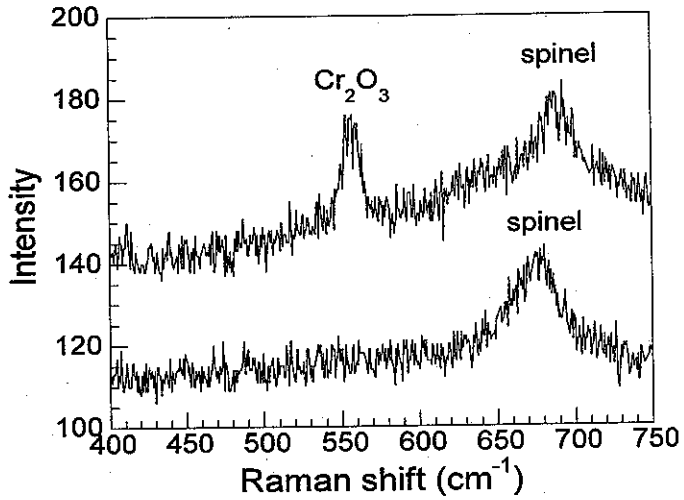

Figure 43. Raman spectra of Alloy 800 at corrosion pits and in area without pits. Specimen was exposed for 810 h to Gas 1 (53.4% H_2-18.4% CO-5.7% CO_2-22.5% H_2O) at 593°C and 15 atm.

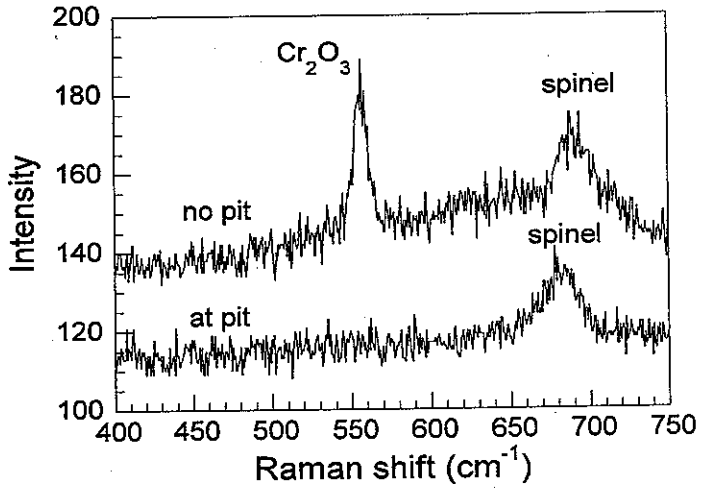

Figure 44. Raman spectra of Alloy 310 at corrosion pits and in area without pits. Specimen was exposed for 810 h to Gas 1 (53.4% H_2-18.4% CO-5.7% CO_2-22.5% H_2O) at 593°C and 15 atm.

In the case of Ni-base alloys, virtually neither corrosion nor pitting was observed when they were tested for 240 h at 1 atm. On the other hand, pits appeared on Alloys 601, 690, 617, and 214 after only 160 h exposure at high pressure (Fig. 45). Figure 46 shows the weight loss data for several Ni-based Alloys. All Ni-base alloys were attacked by corrosion during exposure at high pressure, but the corrosion rates for Ni-based alloys are lower than those for Fe-based alloys.

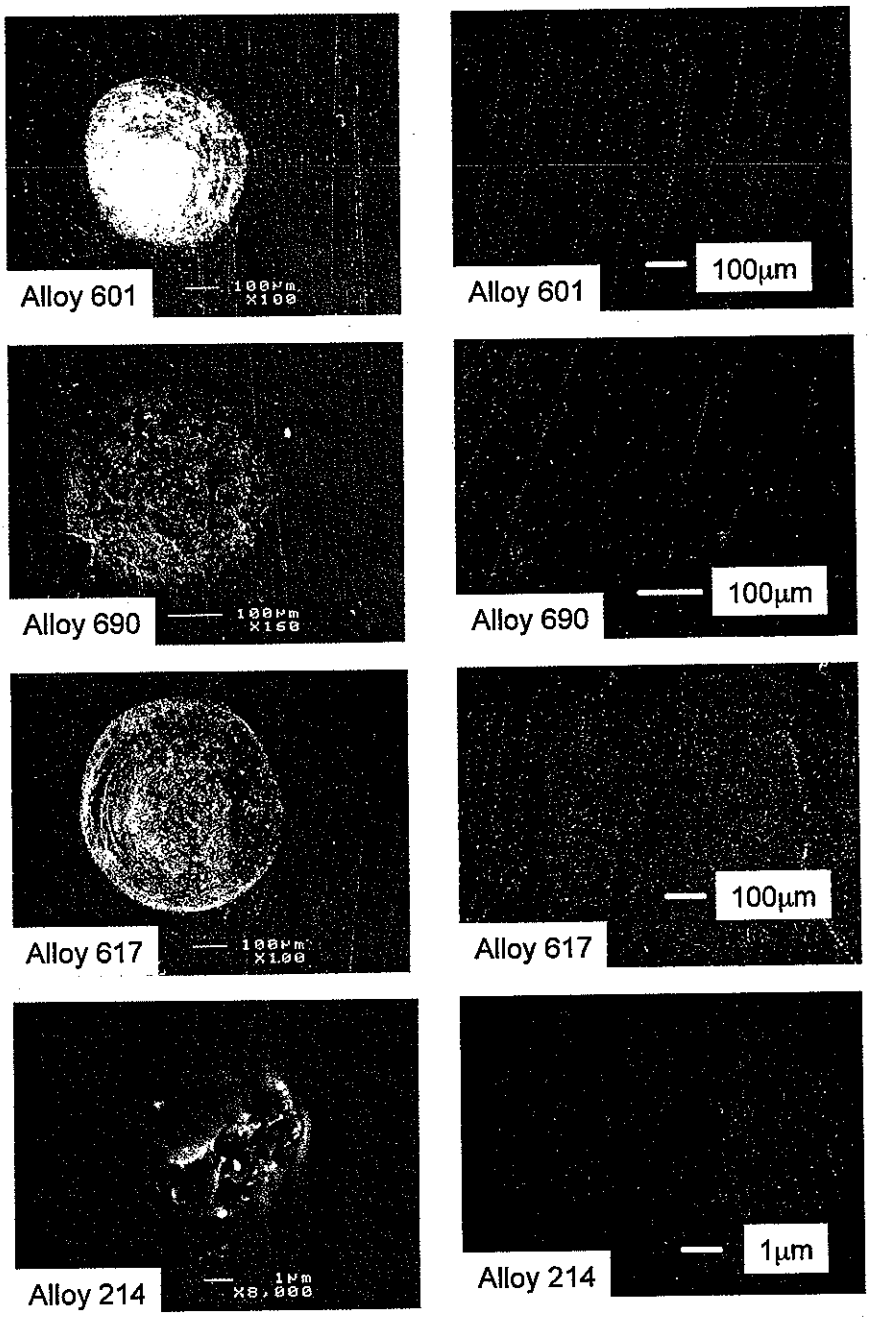

Figure 45. SEM micrographs of Ni-base alloys.
Left: exposed at 15 atm and 593°C for 160 h, pits were observed. Right: exposed at 1 atm and 593°C for 240 h, surfaces of alloys are smooth, and no pits.

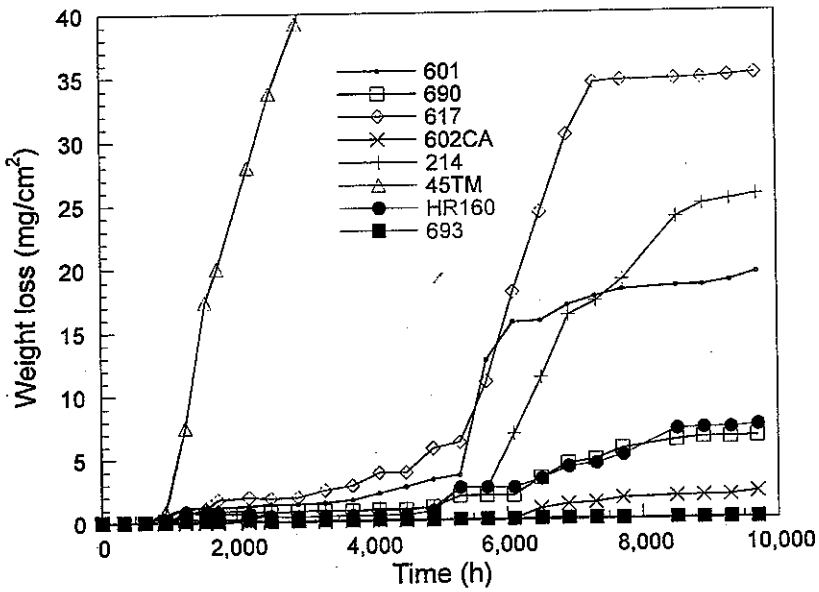

Figure 46. Weight loss data for Alloys 601, 690, 617, 602CA, and 214 exposed to Gas 1 (53.4% H_2-18.4% CO-5.7% CO_2-22.5% H_2O) at 15 atm and 593°C.

In conclusion, metallic interconnects in SOFC can be subjected to corrosion at elevated temperatures and the extent of attack will be influenced by temperature, gas chemistry, and system pressure. Deep pits were observed on several high temperature Fe-base alloys. The oxide scale, consisting predominantly of Cr_2O_3, can protect the alloys from continuing corrosion. Spinel phase in the oxide scale is not as beneficial as Cr_2O_3. High steam content in the gas environment increases the oxygen partial pressure and thereby, increases the stability of the spinel phase, which is less protective; however, the carbon activity also decreases with increasing steam content. Overall, high steam content may be beneficial from the corrosion standpoint and this needs further study, especially at temperatures >600°C. Ni-base alloys develop less spinel phase in the oxide scale and perform better than the Fe-base alloys and corrosion becomes severe only in low-steam and high-pressure environments.

5. REDUCTION OF AREA RESISTANCE OF METALLIC INTERCONNECT

In recent years, we have applied scanning electron microscopy, X-ray diffraction, X-ray near edge absorption spectroscopy, magnetic force microscopy, and copper indicator technique to conduct an in-depth analysis of the oxide layers on surfaces of commercial and newly developed alloys after exposure in oxygen-carbon environments. Results from all these approaches validated the presence of metallic nanoparticles in the oxide scales.

These metal nanoparticles can join to form channels for the transport of carbon through the oxide and degrade the protective capacity of the oxide against further corrosion. This finding may also influence the selection and long-term performance of metallic interconnects materials for SOFCs. For example, currently, solid oxide fuel cell requires adequate electrical conductivity of oxide scale on alloys for viability as interconnect. If we can control the formation of the cluster of metal particles in oxide

scale, we may lead to electrical short through oxide scale and greatly reduce the area resistance of metallic interconnects. On the other hand, if we can prevent the formation of metal particles in oxide scale, the carburization issues may be greatly retarded after removing the carbon transfer channels.

To illustrate the oxidation performance and the details of the oxide scale, we examined specimens of Type 321 stainless steel after exposure at ≈15 atm and 593°C to Gas 1 consisting of 53.4% H_2-18.4% CO-5.7% CO_2-22.5% H_2O. Pits were observed on the alloy surface as shown in Fig. 47a. After exposure, the specimen was cut and a metallographic mount of cross section was prepared and X-ray nanobeam was scanned across the cross section at both the pit and non-pit areas from surface to interior of the alloy. Generally, strong diffraction from Fe/Ni metal phase was observed in oxide scale of non-pit area (Fig. 1 center). The diffraction peak position of the metal particles in oxide scale is different from the peak position of the alloy, which indicates that the lattice parameter of these embedded metal particles in the scale are different from the metal particles in the substrate alloy. Alloy 321 has an austenitic structure with a diffraction peak at 41.1° (d-space at 2.08Å) when the X-ray beam energy is at 8.5 KeV. However, the metal particles in oxide scale showed a ferritic structure with a diffraction peak at 42.1 (d-space at 2.03Å). Portions of the alloy transform from austenitic to ferritic structure near the interface between the alloy and oxide scale. The diffraction intensity from the austenitic phase is stronger than that of the ferritic phase near oxide scale at non-pit area, but it is reverse at the pit area. Both (Fe,Cr) spinel and Cr_2O_3 phases were observed at non-pit area. There were two layers in the oxide scale at pit area and only spinel phase was observed in both layers. No diffraction from metal particles and Cr_2O_3 was seen in the oxide scale at pit area.

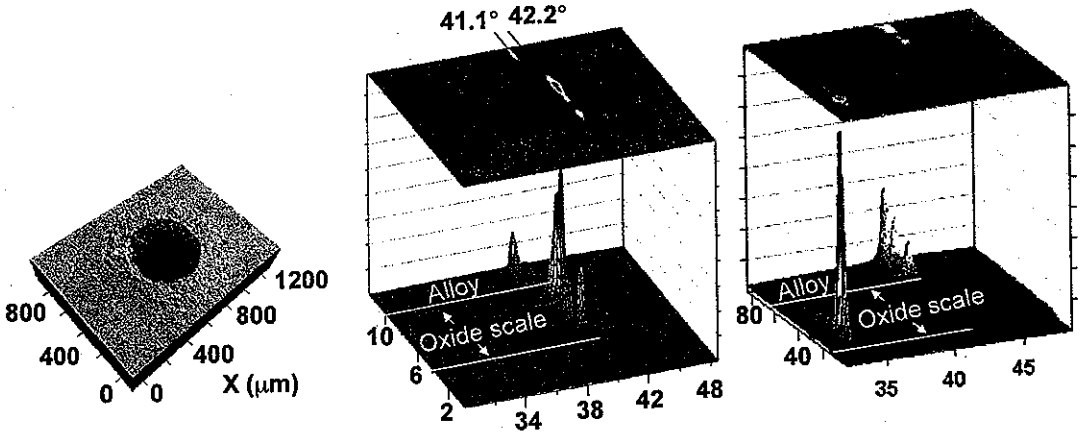

(a) (b) (c)

Figure 47. X-ray nanobeam analysis of Alloy 321.
(a) Left: 3–D profile map of a pit on the surface of Alloy 321.
(b) X-ray diffraction of the oxide scale at the non-pit area.
(c) X-ray diffraction of the oxide scale at the pit area.

EDX analysis was also performed on the cross section of Alloy 321. The thickness of oxide scale at non-pit area is only a few micrometers whereas the

thickness of scale at pit area is over 50 μm. Bright spots in sizes ranging from several tens of nanometers to 800 nm were observed in the SEM image of oxide scale at the non-pit area (see Fig. 48). EDX analysis indicated that these bright spots are rich in iron and nickel, but contained less oxygen and chromium. There is no such bright spot in the oxide scale at pit area of Alloy 321, but two distinct layers were observed in the oxide scale. EDX analysis indicated more oxygen and iron in the outer layer than in the inner layer, but the concentration of chromium and nickel were less in the outer layer than in the inner layer (Fig. 48).

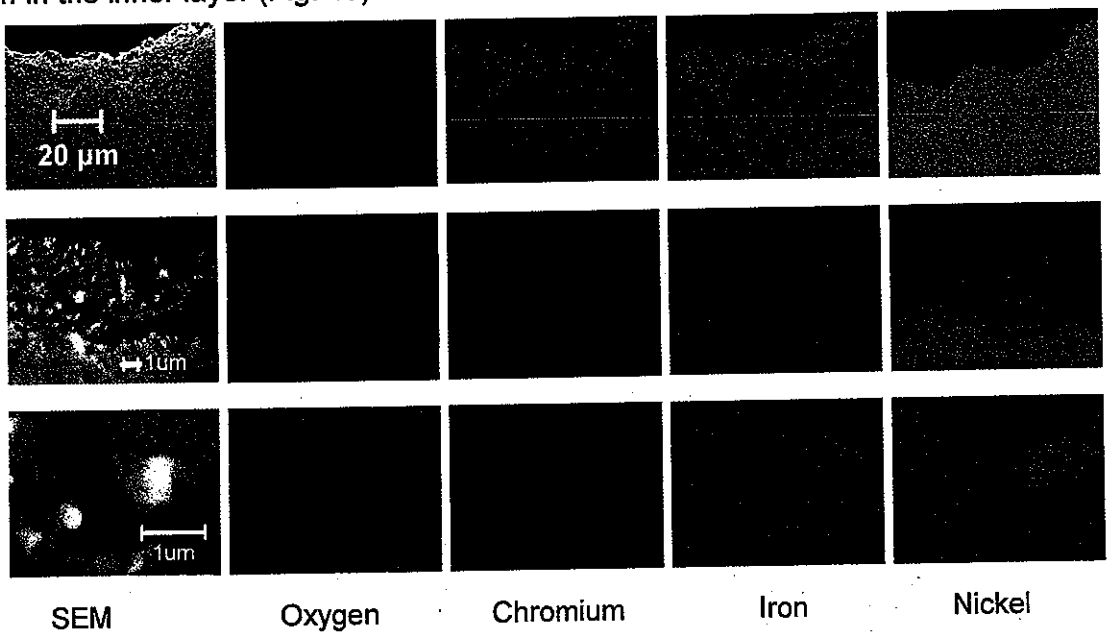

Figure 48. EDX mapping of the cross section at pit and non-pit areas of Alloy 321, after 1130-h exposure in oxygen-carbon environment.
Top row: at the pit area. Middle row: at non-pit area.
Bottom row: enlarged mapping of the bright spots in the image of the middle row.

Atomic force microscope has been used in corrosion research and interested results have been achieved.[30,31] In this report, we present the application of magnetic force microscope to study the ferromagnetic particles in oxide scale. Ferrite phase Fe/Ni particles should be ferromagnetic, whereas $FeCr_2O_4$ and chromium oxide in oxide scale should be paramagnetic at room temperature. The magnetic moment of ferromagnetic Fe/Ni particles should be stronger than that of oxides in the oxide scale. Therefore, we use magnetic force microscope scanned through the area that there are bright spots, which may be Fe/Ni particles. Figure 49 shows that strong magnetic contrast is observed. Although the MFM image is not totally match the SEM image because of the distortion of magnetic domain orientation, this result clearly indicated that there are ferromagnetic Fe/Ni particles with ferrite phase in oxide scale.

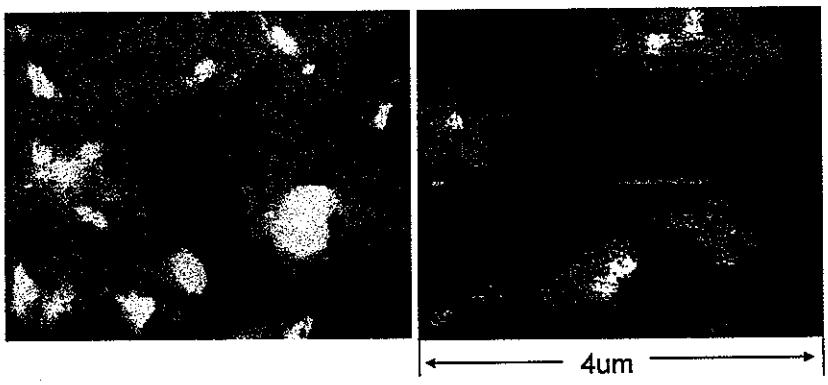

Figure 49. Magnetic contrast image of oxide scale at non-pit area of Alloy 321.

The metal-dusted specimen was also analyzed by nanobeam X-ray fluorescence. In the pit area of the specimen, more iron in the outer layer of the oxide and more chromium in the inner layer were observed (see Fig. 50a). It is surprising that the nickel content in the inner layer of the scale is higher than that in the substrate alloy. This result was also confirmed by EDX analysis but EDX could not establish the valence of the nickel in oxide scale. On the other hand, nanobeam X-ray near edge absorption analysis showed that the chemical shift of nickel in most locations of the oxide scale is close to metallic nickel (see Fig. 50b). This indicates presence of metallic nickel particles in oxide scale. These particles seem to act as channels for the transport of carbon into the alloy.

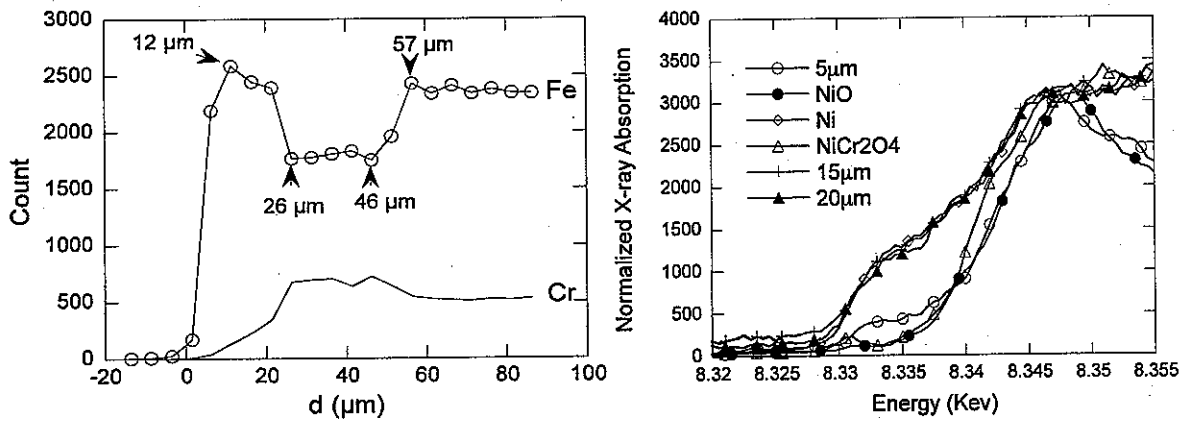

(a) (b)

Figure 50. (a) Nanobeam X-ray fluorescence of oxide scale as a function of scale depth and (b) X-ray near edge absorption spectra (XNEAS) of nickel. The X-ray nanobeam was scanned across the oxide scale to the metal. The positions of 5 μm and 15 μm are at the outer layer of the oxide scale.

Nickel 2+ was observed at the outer layer of the oxide scale at the position close to surface. Although pure $NiCr_2O_4$ is not stale in the reducing environment, small amount of Ni^{2+} may enter the site of Fe^{2+} in $FeCr_2O_4$ to form $(Fe,Ni)Cr_2O_4$ solid solution. The maximum concentration of Ni^{2+} in the solid solution could be calculated from thermochemical data. Using the ΔH and ΔS values of are -5.309 kJ/mole and 16.7J/mole K , respectively, for the formation of $NiCr_2O_4$ from NiO and Cr_2O_3 phases

and the oxygen partial pressure of 4×10^{-24} atm in Gas 10 at 14.3 atm and 593°C, the calculated value for the maximum concentration of Ni^{2+} in spinel phase is 15.2%. The oxygen partial pressure at the oxide/substrate interface, based on Cr/Cr_2O_3 equilibrium for an alloy with 18 wt.% Cr, is 2.5×10^{-36} atm which is much less than in the bulk gas. Therefore, the calculated value for the minimum concentration of Ni^{2+} (corresponding to the pO_2 established by $Cr\text{-}Cr_2O_3$ equilibrium) is only 1.2×10^{-5}%. These results indicate that the concentration of Ni^{2+} in spinel should be high at the gas side of the oxide scale, and it should be low in the oxide on the alloy side of the scale.

In the early stage of oxide scale formation, nickel could be oxidized to +2 at the gas-oxide surface and dope into the solid solution of $(Fe,Ni)Cr_2O_4$. The Ni^{2+} in the solid solution could be as high as 15.2%. When cations continue to diffuse out, the nickel containing spinel was buried inside. The pO_2 in the inner layer of oxide scale decreases with increasing thickness of the oxide scale and Ni^{2+} will be reduced to nickel metal when the pO_2 drops below the critical value. Such a process leads to the formation of nickel particles in oxide scale. $FeCr_2O_4$ spinel itself is not stable either. The equilibrium pO_2 near boundary of oxide to alloy is low enough to reduce $FeCr_2O_4$ to iron and Cr_2O_3. Iron particles can also be present in the oxide scale. Therefore, formation of the metallic nano-particle occurs due to the reduction of nickel and iron ions in spinel phase during the growth of the oxide scale.

The results from X-ray nanobeam analysis indicate that the oxide scale in the pit region is actually a mixture of oxide and metal particles. These metal particles can lead to preferential channels for the inward diffusion of carbon. However, nickel oxidation and reduction process will occur if iron is present in alloys because pure $NiCr_2O_4$ spinel will not form in the reducing environment. Only when $FeCr_2O_4$ forms, Ni^{2+} can dope into iron-containing spinel to form $(Fe,Ni)Cr_2O_4$ solid solution. In the absence of iron, nickel will not be subjected to the oxidation-reduction process. Therefore, the spinel phases in oxide scale cause problems by forming unstable iron-rich phase and act as a solvent for the formation of Ni^{2+}, and the Ni^{2+} will be reduced to nickel metal (over long time) enabling formation of carbon transfer channels.

According to above analysis, carbon attack would be greatly retarded if alloys can develop an oxide scale that consists of only chromium oxide. Therefore, we designed and prepared several nickel base alloys with low iron contents. The chromium content of Alloy ANL-1 (74.5% Ni, 22% Cr, 2.3%Al, 0.7% Fe, 0.3% Ti, 0.2% Zr, and 0.1% C) is similar to commercial alloy 601 (61.8% Ni, 21.9% Cr, 1.4%Al, 14.5% Fe, 0.3% Ti, 0.1% Nb, and 0.03% C. However, the Raman scattering spectra indicates that spinel phase formed on surface of commercial alloy 601 but not on the surface of low-iron alloy when the samples were exposed for 12,858 h in a carburizing gas consisting of 65.1% H_2-4% CO_2-30% CO-0.9% H_2O at 1atm and 593°C (Fig. 51). Pits were observed on Alloy 601 within 1,000 h exposure. Although the composition of ANL-1 is close to Alloy 601 except the low iron content in ANL-1, its incubation time for corrosion is much longer than that of Alloy 601. No pitting occurred on ANL1 alloy even after 12,858 h exposure in the same environment. This result indicates that carbon has not

broken through the non-spinel oxide scale on ANL-1 alloy, but it is easy to penetrate through the scale containing spinel phase on commercial Alloy 601.

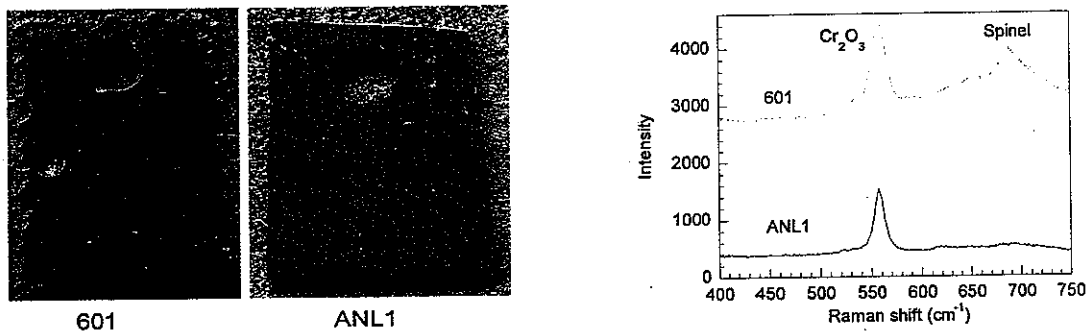

Figure 51. Macrophotographs and Raman spectra of Alloys 601 and ANL-1 after 12,858-h exposure to the same metal dusting environment at 593°C and 1 atm.

Metal nano-particles were also observed in the oxide scale of other alloys and in other test environments. Figure 52 shows the cross section of oxide scale on Alloy 310 (Fe-19.5%Ni-25.5%Cr-52-1.7%Mn-0.7%Si-0.03%C) after 1636-h exposure to a carburizing gas consisting of 65.1%H_2-4%CO_2-30%CO-0.9%H_2O at 1atm and 593°C. Pits were observed after the short exposure period, even though the chromium content in this alloy is high. The density of metal particles in oxide scale in the pit area is higher than that at non-pit area. Metal particles form nano-wires and were oriented perpendicular to the alloy surface. An almost continuous channel of metal particles was observed from the surface through the oxide scale to the substrate alloy and enables transport of carbon. The oxygen atoms being much larger than carbon, its transport through these channels is probably insufficient to form a continuous oxide scale. In the non-pit regions, the particles may not have formed continuous channels and the orientation of the metal clusters probably is parallel rather than perpendicular to the alloy surface, thereby resulting in less metal dusting attack. The figure also shows a schematic representation of possible orientation of carbon-transfer channels in the two regions.

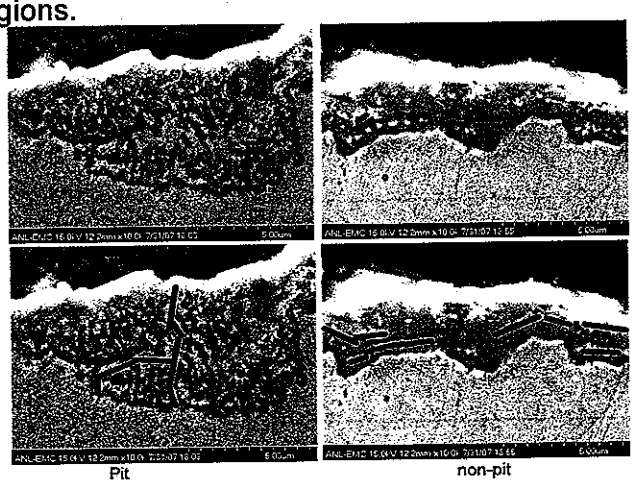

Figure 52.
top: SEM cross section image of pit and non-pit area on Alloy 310 after 1,636-h exposure to carburizing gas consisting of 65.1% H_2-4% CO_2-30% CO-0.9% H_2O at 1atm and 593°C.
bottom: The possible carbon transfer channels were indicated by black lines in the image.

Because the electrical conductivity of metallic nickel and iron is 100 million times higher than that of spinel,[32] the electrical resistivity of the oxide scale at pit area will be much lower than that at non-pit area if metal clusters connect to form channels in the pit area. The procedure for detecting the low-resistance area on the surface of alloys is to deposit metal (such as copper) particles by an electrochemical method in which copper is deposited on the alloys by immersing them in the $CuSO_4$ solution and applying a voltage across the electrodes (Fig. 53a). The areas with low resistance will have deposits of copper particles because current can pass through them. Deposited copper particles thus act as an indicator to locate the carbon transfer channels. Figure 53b shows the copper-deposited region of a pit on the surface of Alloy 310. Such areas can also be identified under a microscope and probably indicate regions of active degradation. Figure 53b shows that the density of the deposited copper at the pit area is much higher than that at non-pit area. This experiment confirmed that the electrical resistance of the pit area is much lower than that of non-pit area because the metal nano-particles at the pit area have connected to each other through the oxide scale but the metal nano-particles is isolated at the non-pit area.

Self-assembled metallic network in oxide scale at a pit area of alloy 353MA was also observed (Fig. 54). It seems that these networks form from the grain boundary of $(Fe,Ni)Cr_2O_4$ spinel. When the spinel was buried inside and decomposed the ductile nickel particles was depleted from the grain and pushed into the grain boundary to form such a metallic network.

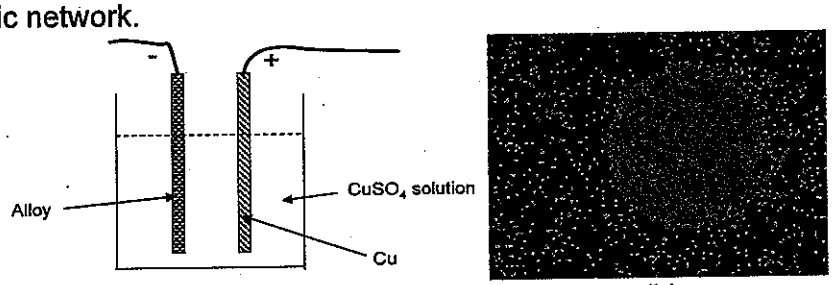

Fig. 53. (a): Setup for electrochemical deposition of copper.
(b): copper-deposited region of a pit on the surface of Alloy 310.

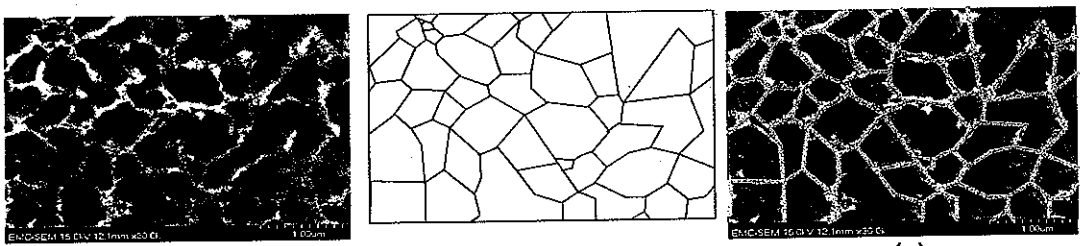

Figure 54. (a) SEM cross section image of pit and non-pit area on Alloy 353MA after 1,636-h exposure to carburizing gas consisting of 40.2% H_2-0.2% CO_2-19.8% CO-0.1% H_2O-39.7% N_2 at 1atm and 593°C.
(b) Possible grain boundary of spinel in oxide scale on Alloy 353MA.
(c) Superimposition of (a) and (b).

6. IMPROVEMENT IN ELECTRICAL CONDUCTIVIRY OF SURFACE OXIDES

Generally, Cr and Al-containing alloys are selected for application as interconnect at high temperature in SOFCs, because the oxidation rates can be low leading to thin oxide scales. However, oxide scales have high resistance and can decrease the ability of metallic interconnect to conduct electric current between fuel cell stacks. Area specific resistance of oxidized Cr-containing alloys is generally lower than that of alumina-forming alloys, since the resistivity of Cr_2O_3 is much lower than that of Al_2O_3. Even though research has focused on Cr_2O_3-forming alloys, chromium oxide evaporation can lead to several issues in acceptable performance of SOFCs. Chromium oxide vapor may react with solid state electrodes and electrochemical reduction of CrO_3 at cathode/electrolyte/gas phase boundary can lead to polarization losses. A significant transport of chromium from alloys to electrodes has been reported.[22] Reaction between the electrodes and metallic interconnect causes degradation in cell performance.[21] Al-containing alloys have much better ability to resist oxidation than Cr-containing alloys and Al_2O_3 scale growth rate is ten times lower than that of Cr_2O_3. However, Al-containing alloys have almost been abandoned for metallic interconnects, since the resistance of the Al_2O_3 scale is too high. If metallic nanowires can be grown through the alumina scale, the resistance of the alumina scale can be dramatically reduced.

Figure 55 shows the possible scale structure during oxidation of aluminum containing alloys. Alumina scale usually grows as an inner layer between the outer layer of scale and the alloy substrate where the oxygen partial pressure is low. Alumina can also form compounds with other oxides leading to $NiAl_2O_4$ and $CuAl_2O_4$ formation when exposed in air at high temperatures. If we add copper to the alloys and carefully control the temperature and gas composition, $NiAl_2O_4$ and $CuAl_2O_4$ may form on surface of alloy at the initial exposure. When the scale grows by outward transport of cations such as Fe and Cr, $NiAl_2O_4$ and $CuAl_2O_4$ will be buried inside the oxide scale. As the scale grows, the oxygen partial pressure will decrease inside the scale towards the alloy and phases such as $NiAl_2O_4$ and $CuAl_2O_4$ will become unstable and finally decompose to form the alumina scale with copper metallic network as shown in Fig. 55. Since elements such as nickel and copper will not oxidize at low oxygen partial pressure prevalent in the interior of scale, the inner layer of the scale would consist of Al_2O_3-Cu or Al_2O_3-Ni mixture that can still protect the alloy from continued oxidation. However, the electric resistance of such a tailored scale will dramatically drop.

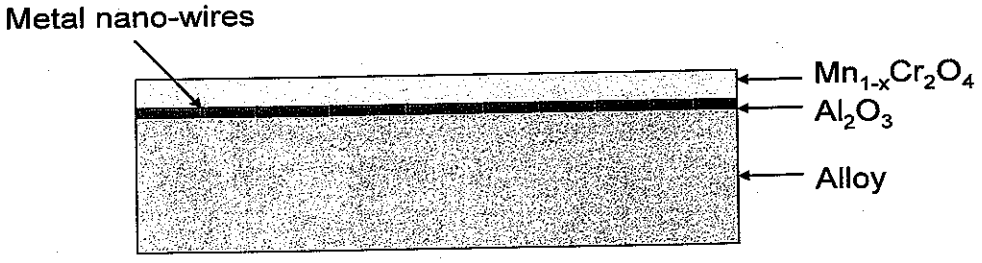

Figure 55. Schematic of a tailored scale to reduce electrical resistivity of the thermally grown scale.

To examine the approach proposed above, we have prepared several nickel-base alloys with aluminum and copper additions. Table 4 shows the chemical composition of two of the alloys. These alloys showed excellent oxidation resistance at 800°C (Fig. 56). The weight gain rates of these alloys are smaller than the alloys without aluminum addition (Fig. 57). Table 5 shows the area specific resistance of typical Cr_2O_3-forming alloys and ANL-developed aluminum added alloys. Area specific resistance of ANL-developed alloys is much lower than those of both Alloy 446 and Crofer (Fig. 58), although the ANL-developed alloys were exposed to air at 800°C for much longer time. This result indicates that it is possible to reduce the area resistance of metallic interconnect with controlled addition of aluminum. Additional studies are needed to evaluate the performance of these types of alloys in simulated fuel cell environments at projected operating conditions of the cell.

Table 4. Composition of ANL-developed alloys.

Alloy Designation	Composition (in wt.%)							
	Ni	Cr	Al	Ti	Zr	C	Cu	Fe
ANL-1	65.2	22	2.3	0.3	0.2	0.1	10	<0.1
ANL-2	75.2	22	2.3	0.3	0.2	0.1	-	<0.1

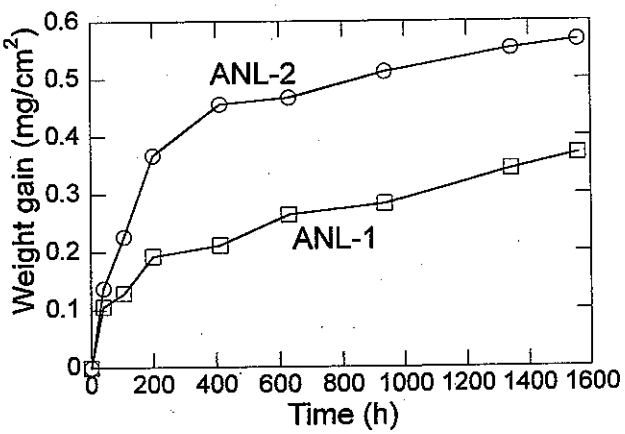

Figure 56. Weight gain of ANL-developed Ni-based alloys after exposure in air at 800°C.

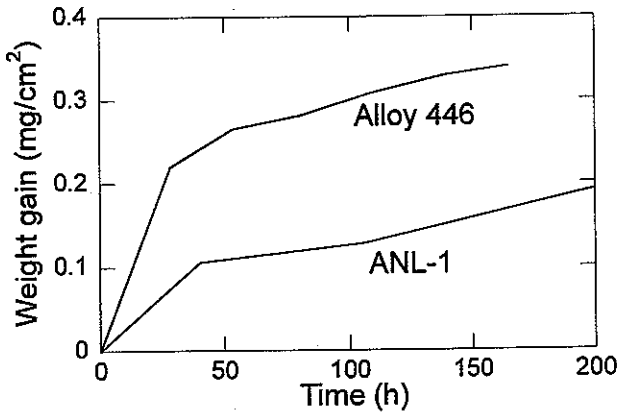

Figure 57. Weight gain of Alloy 446 and ANL-developed Ni-base alloy in air at 800°C.

Table 5. Area specific resistance of alloys at 800°C.

Alloys	Crofer	446	ANL-1	ANL-2
Time (h)	328	1000	1550	1550
ASR ($m\Omega \cdot cm^2$)	340	130	29	31

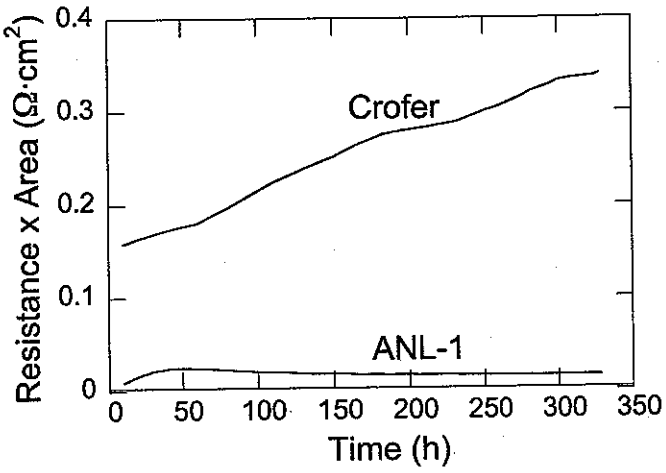

Figure 58. Area specific resistance of Alloy Crofer and ANL-developed alloy.

Doping of mixed valence elements into alumina scale may be another approach to reduce the electric resistance of the scale. The resistivity of Al_2O_3 is 2.5×10^8 Ω·cm at 900°C. However, the resistivity of $MnAl_2O_4$ is only one ten thousandth of the resistivity of Al_2O_3[33], and the resistivity of the manganese aluminum spinel could be further reduced by increasing the Mn content in $Mn_{(1+x)}Cr_{(2-x)}O_4$. Mn is +2 in $MnAl_2O_4$ and if more Mn ions are doped into the spinel, Mn will be mixed valence of Mn^{2+}/Mn^{3+} in $Mn_{(1+x)}Al_{(2-x)}O_4$. Generally, resistivity decreases dramatically when mixed valence state is present in solid oxides. For example, the resistivity of $Mn_{(1+x)}Cr_{(2-x)}O_4$ decreases from 1950 Ω.cm for x=0 to 3.3 Ω·cm for x=1.[25] Therefore, it may be possible to decrease the resistivity of $Mn_{(1+x)}Al_{(2-x)}O_4$ spinel to values similar to the resistivity of Cr_2O_3 ($\approx 10^2$ Ω·cm at 800°C), if we adjust the concentration of the dopant Mn.

The valence of ions of transition metals depends on the oxygen partial pressure (pO_2) that decreases from the surface to alloy substrate. Therefore, several transition metals such as Mn, Ti, V, Zr, and Ce could be used as doping elements. These elements exhibit multiple valence states that may be stable in different ranges of pO_2. These doping elements, if tailored, may lead to electron transfer channels through the oxide scale, thereby, reduce the area specific resistance of the oxide scale on Al_2O_3-forming alloys.

Y_2O_3 particles have been successfully dispersed into alloys to improve the adhesive of oxide scale to alloys. Using a similar approach, the electrical conductivity of oxides can be improved by dispersion of conducting fibers into candidate interconnect alloys. When Al_2O_3 scale forms, the conducting fibers on alloy surface would cut across

the oxide scale and conduct electric current from electrodes to substrate alloy. A conductive coating layer, for example, of La(Sr)MnO_3 would connect individual conductive fibers and assist in the transport of electric current from electrodes to oxidized alloys.

The resistivity of $CeAlO_3$ is five orders of magnitude lower than that of Al_2O_3[34] and close to the resistivity of Cr_2O_3 at 800°C. Doping of the above-discussed elements could further reduce the resistivity. One of the approaches is to prepare nano-size powder or fibers of $CeAlO_3$ and disperse these powders/fibers into Al_2O_3-forming alloys. The conductive powders/fibers may lead to electrical short circuit paths through the oxide scales and reduce the area specific resistance of Al_2O_3-forming alloys, as shown in Fig. 59.

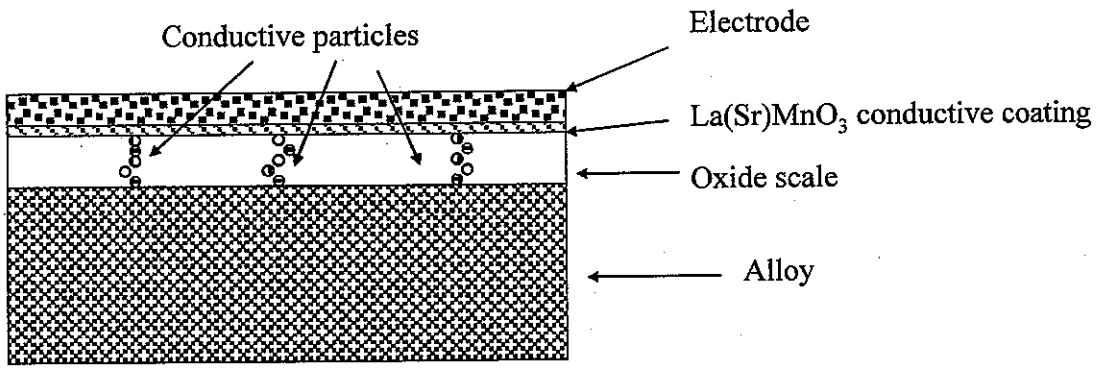

Figure 59. Schematic of an approach to improve electrical conductivity of thermally grown oxide scales.

7. SUMMARY

We have examined five topics of interest for the development of metallic interconnects with adequate performance in fuel cells for long service life. In recent years, an extensive program was conducted at Argonne National Laboratory to establish the mechanisms for degradation of metallic materials exposed to hydrocarbon- and oxygen-bearing gaseous environments, to identify the key parameters that influence the onset of corrosion and propagation of degradation, to establish the metal wastage under a variety of exposure conditions, to characterize the morphology of degradation using a wide variety of analytical techniques, and to assess the effect of alloy chemistry, carbon activity and oxygen partial pressure, and system pressure on the extent of corrosion. This report presents fuel-cell relevant research conducted over the years and the conclusions reached and were used to identify additional areas of research on materials for improved performance of components, especially metallic interconnects, in the complex fuel cell environments.

This report details research conducted in the following areas: measurement of area specific electrical resistivity, corrosion performance in dual gas environments by experiments using alloy 446, long term corrosion performance of ferritic and austenitic

alloys in hydrogen and methane-reformed synthesis fuel-gas environments, approaches to reduce the area resistance of metallic interconnect, and reduction of electrical resistivity of alumina scales on metallic interconnect.

Since the alloys acceptable for interconnect application contain a high concentration of chromium (to posses adequate mechanical strength), they generally develop chromia or chromia-rich scales both in air and in fuel-gas environments. Therefore, the electrical conductivity of thermally grown chromia scales is of interest. We have generated electrical conductivity data as a function of temperature and oxygen partial pressure for thermally grown chromia scales measured by four-probe method. The data indicate that at ≈550°C, the conductivity values can range from 3×10^{-4} to 1.8×10^{-3} $\Omega^{-1}\cdot cm^{-1}$ as the pO_2 increases from 10^{-30} atm to 0.21 atm (air). At a temperature of 850°C, the corresponding values are 1.8×10^{-3} and 0.01 $\Omega^{-1}\cdot cm^{-1}$, respectively.

We have used Alloy 446 (a high chromium ferritic steel) to evaluate its corrosion performance in a dual gas environment, pertinent to SOFCs. Alloy 446 tube was exposed to dual gases of air and 2.3% H_2O-H_2 at several temperatures in the range of 500-825°C. The synchrotron nanobeam X-ray diffraction analysis showed that oxide scale on the airside consisted of two layers. The outer layer was predominantly a spinel phase and the inner layer was a mixture of spinel and Cr_2O_3. The oxidation state of Mn in the spinel was between +2 and +3 when the alloy was exposed to air. The mixed valence state led to a lower resistivity for the oxide scale. However, the oxidation state of Mn in the spinel was close to 2 when the alloy was exposed to 2.3% H_2O-H_2 atmosphere. Similar experimental effort and mechanism-based analysis of the surface scales are needed to evaluate the performance of candidate interconnect materials.

We have evaluated the corrosion performance of several Fe- and Ni-base alloys in simulated hydrocarbon containing complex gas environments that are applicable to SOFCs. The metallic interconnects in SOFC can be subjected to corrosion at elevated temperatures and the extent of attack will be influenced by temperature, gas chemistry, and system pressure. In the DOE/Office of Industrial Technologies program conducted at ANL, corrosion information was developed predominantly at 593°C in a wide range of gas chemistry and system pressure. The data showed that the alloy chemistry had a significant effect on its long-term corrosion performance. Deep pits were observed on several high temperature Fe-base alloys. The oxide scale, consisting predominantly of Cr_2O_3, can protect the alloys from continuing corrosion. Spinel phase in the oxide scale is not as beneficial as Cr_2O_3. High steam content in the gas environment increases the oxygen partial pressure and thereby, increases the stability of the spinel phase, which is less protective; however, the carbon activity also decreases with increasing steam content. Overall, high steam content may be beneficial from the corrosion standpoint and this needs further study, especially at temperatures >600°C. Ni-base alloys develop less spinel phase in the oxide scale and perform better than the Fe-base alloys and corrosion becomes severe only in low-steam and in high-pressure environments.

Increasing the Cr content (from 20 to 29 wt.%) in alloys had less effect in decreasing the corrosion rate when compared with the benefit of decreasing the Fe

content in the alloy on the growth rate. The presence of Fe in the alloy leads to formation of (Fe,Cr) spinel phase in the scale. Over time, the Fe/Cr ratio in the spinel increases to essentially make it unstable in the high-carbon environments and eventual breakdown of the protective capacity of the scale. Therefore, we designed and prepared several alloys with low concentration of Fe and tested in carburizing environments. Results showed that the ANL-developed alloys formed predominantly Cr oxide in the scale and the incubation time for corrosion was extended ten times more than that of the commercial alloys with similar chromium contents. These ANL-developed alloys have potential for SOFC interconnect application and needs further study, especially at elevated temperatures.

8. RECOMMENDATIONS FOR FUTURE WORK

Based on the key requirements for metallic interconnects and the data developed on the corrosion behavior of candidate materials in meeting those requirements, several areas are recommended for further research to develop metallic interconnects with acceptable and reliable long-term performance in solid oxide fuel cells. Specifically they are:

- Evaluation of scaling on candidate alloys over a wide temperature range of 500-850°C after exposure to simulated natural gas-reformed effluent and in coal-derived gases that contain hydrocarbons, sulfur species, and possibly chlorine containing compounds.

- Establish the oxide growth rates and electrical conductivity of thermally grown surface oxides that form in complex gas environments.

- Evaluate the effect of dual gas atmosphere on the scaling of candidate alloys as a function of temperature and exposure time. Evaluate the electrical conductivity of the surface layers.

- Effect of gas mixtures that contain a high steam content to simulate the fuel cell downstream environment from the standpoint of scaling, internal oxidation, and electrical properties.

- Evaluate the corrosion performance of the ANL-developed alloys in simulated fuel cell environments and measure the electrical conductivity of the oxide layers.

- Advance materials development by tailoring the surface oxides in chromia-forming alloys with metallic particles and fibers to improve their electrical conductivity.

- Study the development of alumina-forming alloys with emphasis on improvement in its electrical conductivity by dispersion of dopants such as, Mn, V, Ti, Zr, and Ce.

- Develop oxide-based coating to minimize the evaporation of chromium/chromium oxides, to improve the Cr mass transfer thereby, improve the cell performance.

ACKNOWLEDGEMENTS

We thank M. Grimsditch and V. Maroni for their assistance in conducting the Raman analysis, S. Cai for data analysis of the nanobeam X-ray diffraction, and D. L. Rink for his assistance in conducting the metal dusting experiments. We also thank Jan Froitzheim, Julich Research Center, Germany, for his contribution in the study of Crofer alloy and other ferritic steels during his tenure at Argonne National Laboratory. This work is supported by the U.S. Department of Energy, Office of Industrial Technologies. The electron microscopy analysis was accomplished at the Electron Microscopy Center for Materials Research at Argonne National Laboratory, a U.S. Department of Energy Office of Science Laboratory operated under Contract No. DE-AC02-06CH11357 by UChicago Argonne, LLC.

REFERENCES

1. M. C. Wlliams, J. P. Strakey, and W. A. Surdoval, Int. J. Appl. Ceram. Technol. 2, 295, 2005.
2. M. C. Wlliams, J. P. Strakey, and W. A. Surdoval, J. Power Sources, 143, 191, 2005.
3. M. C. Wlliams, J. P. Strakey, and W. A. Surdoval, J. Power Sources, 131, 79, 2004.
4. N. Q. Minh, J. Am. Ceram. Soc. 76, 563, 1993.
5. S. Linderoth, P. V. Hendriksen, M. Mogensen, and N. Langvad, J. Mater. Sci. 31, 5077, 1996.
6. W. Weppner, Proceedings of the International Symposium on Solid Oxide Fuel Cells. Edited by O. Yamamoto, M. Dokia, and H. Tagawa, Science House, Tokyo, Japan, 1990.
7. H. Tenmei, H. Michibata, T. Namikawa, and Y. Yamazaki, Denki Kagaku, 58, 1072, 1990.
8. E. Ivers-Tiffee, W. Wersing, M. Schliessl, and H. Greiner, Ber. Bunsenges. Phys. Chem., 94, 978, 1990.
9. S. de Souza, S. J. Visco, and L. C. De Jonghe, Solid State Ionics 98, 57, 1997.
10. S. de Souza, S. J. Visco, and L. C. De Jonghe, J. Electrochem. Soc., 144, L35, 1997.
11. H. Liu, M. M. Stack, and S. B. Lyon, Solid State Ionics, 109, 247, 1998.
12. T. Brylewski, M. Nanko, T. Maruyama, and K. Przybylski, Solid State Ionics, 143, 131, 2001.
13. K. Huang, P. Y. Hou, and J. B. Goodenough, Mater. Res. Bull. 36, 81, 2001.
14. W. J. Quadakkers, T. Malkow, J. Piron-Abellan, U. Flesch, V. Shemet, and L. Singheiser, Materials and Components, 150, 1, 2001.
15. R. F. Hochman, Proc. Symp. on Properties of High-Temperature Alloys with Emphasis on Environmental Effects, Z. A. Foroulis and F. S. Pettit, eds., The Electrochemical Society, pp. 715-732, 1977.
16. H. J. Grabke, Materials and Corrosion, 49, 303, (1998)
17. M. Ueda and H. Taimatsu, Materials and Components, 150, 3, 2001.
18. K. Natesan and Z. Zeng, "Development of Materials Resistant to Metal Dusting Degradation," Argonne National Laboratory Report, ANL-06/14, 2005.
19. K. Natesan and Z. Zeng, "Development of Materials Resistant to Metal Dusting Degradation," Argonne National Laboratory Report, ANL-07/30, 2007.
20. P. Kofstad and R. Bredesen, Solid State Ionics, 52, 69, 1992.

21. S. P. S. Badwal, R. Deller, K. Foger, Y. Ramprakash, and J. P. Zhang, Solid State Ionics, 99, 297, 1997.

22. W. J. Quadakkers, H. Greiner, M. Hansel, A. Pattanaik, A. S. Khanna, and W. Mallener, Solid State Ionics, 91, 55, 1996.

23. K. Hilpert, D. Das, M. Miller, D. H. Peck, and R. Weiss, J. Electrochem. Soc., 143, 3642, 1996.

24. J. H. Park and K. Natesan, Oxidation of Metals, 33, Nos.1/2, 31,1990.

25. W. Qu, L. Jian, J. M. Hill, and D. G. Ivey, J. Power Sources, 153,114, 2006.

26. Z. G. Yang, M. S. Walker, P. Singh, and J. W. Stevenson, Electrochem. Solid State Lett. 6, B35, 2003.

27. Z. G. Yang, M. S. Walker, P. Singh, J. W. Stevenson, and T. Norby, Electrochem. Soc., 151, B669, 2004.

28. Z. Zeng and K.Natesan, Solid State Ionics, 167, 10, 2004.

29. D. Thierry, D. Persson, C. Leygraf, D. Delichere, S. Joiret, C. Pallotta, and A. Hugot-Le Goff, J. Electrochem. Soc. 135, 305, 1988.

30. M. Stratmann and M. Rohwerder, Nature, 410, 420, 2001

31. J. Erlebacher, M. J. Aziz, A. Karma, N, Dmitrov, and K. Sieradzki, Nature, 410, 450, 2001.

32. P. C. Thayer, Thesis for Degree of Doctor of Philosophy, Colorado State University, Fort Collins, Colorado, 1972.

33. S. J. Backs and T. H. Etsell, Solid State Ionics, 53, 1305, 2006.

34. I. Shelykh and B. T. Melekh, Phys. Soild State, 45, 248, 2003.

Nuclear Engineering Division
Argonne National Laboratory
9700 South Cass Avenue, Bldg. 212
Argonne, IL 60439-4838

www.anl.gov

A U.S. Department of Energy laboratory
managed by UChicago Argonne, LLC